Struct Multidisc Optim (2018) 57:1187–1211
https://doi.org/10.1007/s00158-017-1804-3

RESEARCH PAPER

Form-finding of grid-shells using the ground structure and potential energy methods: a comparative study and assessment

Yang Jiang[1] · Tomás Zegard[2] · William F. Baker[3] · Glaucio H. Paulino[1]

Received: 8 May 2017 / Revised: 26 August 2017 / Accepted: 31 August 2017 / Published online: 8 November 2017

Abstract The structural performance of a grid-shell depends directly on the geometry of the design. Form-finding methods, which are typically based on the search for bending-free configurations, aid in achieving structurally efficient geometries. This manuscript proposes two form-finding methods for grid-shells: one method is the potential energy method, which finds the form in equilibrium by minimizing the total potential energy in the system; the second method is based on an augmented version of the ground structure method, in which the load application points become variables of the topology optimization problem. The proposed methods, together with the well-known force density method, are evaluated and compared using numerical examples. The advantages and drawbacks of the methods are reviewed, compared and highlighted.

Keywords Form-finding · Grid-shells · Potential energy method · Ground structure method

Yang Jiang and Tomás Zegard equally contributed.

✉ Glaucio H. Paulino
paulino@gatech.edu

[1] School of Civil & Environmental Engineering, Georgia Institute of Technology, 790 Atlantic Drive, Atlanta, GA 30332, USA

[2] Pontificia Universidad Católica de Chile, Vicuña Mackenna 4860, Santiago, RM 7820436, Chile

[3] Skidmore, Owings & Merrill LLP, 224 S Michigan Ave, Chicago, IL 60604, USA

1 Introduction

The present work introduces two form-finding methods for grid-shells: one method based on the minimization of potential energy, dubbed as the *potential energy method* (PEM); and a second method based on an augmented form of the *ground structure method* (GSM) (Dorn et al. 1964). The main advantage of the potential energy method is the reliance on all equations of mechanics (kinematics, equilibrium, and constitutive relations), all of which have direct physical interpretation. On the other hand, the ground structure method approximates the absolute optimal shape (with no dependence on additional user-supplied parameters).

From the aforementioned, the PEM can be considered as a stiffness-type method, since it not only considers force equilibrium, but the constitutive and compatibility equations as well. However, it does not make direct use of the stiffness matrix: instead, it minimizes the potential energy of the system considering large deformations. It is therefore akin to the experimental approach originally used by Gaudí and Isler (Bergós and Llimargas 1999; Chilton 2010). The problem of potential members in compression (when seeking a tension-only solution) (Haber and Abel 1982), is solved by relaxing the stiffness to trigger the snap-through process of these members.

The (augmented) ground structure method's core idea consists of replacing the topology, shape and sizing problem by a sizing-only problem (Hemp 1973). This sizing-only problem is done for a highly-redundant and interconnected truss system (i.e. the ground structure), from which the optimal layout is extracted and sized. The standard formulation of the method is augmented to include the load application points as variables of the problem, thus making the

method suitable for the form-finding of compression-only structures (no need to *flip* the result). The proposed method considers the iterative refinement of the initial ground structure based on previous results, thus increasing the degree of precision of the resulting geometry. The method can be performed over any (discretized) footprint thanks to a graph-theory based generation algorithm (Zegard and Paulino 2014, 2015), and requires no a priori connectivity or sizing. The resulting (optimal) geometry is highly precise; but the lattice-like underlying structure does require a posteriori interpretation or rationalization to finalize the design.

The rest of the manuscript is organized as follows: Section 1.1 reviews the literature in the field of form-finding; Section 1.2 briefly reviews the well-known force density method (for the purpose of completeness and comparison); Section 2 describes the various types of static loads that are considered in the form-finding process; Section 3 is dedicated to the form-finding method based on the principle of minimum potential energy; Section 4 introduces the form-finding method using the augmented ground structure method; Section 5 shows three numerical examples designed with the three form-finding methods previously presented; Section 6 discusses the features of the two proposed form-finding methods and the force density method; Finally, a summary and comparison of these methods, as well as concluding remarks are given in Section 7. Appendix A has details on the formulation of the force density method, and Appendix B presents the nomenclature used in the main text of this manuscript.

1.1 Literature review

Grid-shells are a type of compression-only structure, where efficiency is attained by minimizing (or ideally eliminating) the bending moment and shear forces. Optimal compression-only designs can be analytically derived under specific conditions of loads and geometry. However, in most practical applications a compression-only design cannot be obtained analytically. Early works in form-finding can be traced back to the experimental models used by Antoni Gaudí: the form for the *Colonia Güell* was obtained using a scaled experimental model consisting of hanging chains and weights, which he called a *funicula* (or funicular) model. This model was continuously revised for 10 years; adjusting the cord lengths and hanging weights (Bergós and Llimargas 1999; Martinell et al. 1975). The results from this experimental model were mirrored vertically, and traced over for further graphical refinement in order to obtain a compression-only solution (Collins 1977). An analogous concept was later used by Frei Otto, but using soap film models instead of hanging chains (Addis 2007). Heinz Isler, used hanging cloths to overcome the difficulties of soap films, and used this experimental technique to design impressive thin shell concrete structures (Chilton 2010).

With the rise of computers, new (computational) form-finding methods replaced the previous experimental approach using scaled models. One said method consists of constructing the stiffness matrix using the elastic constitutive equations, and solving for a configuration in equilibrium for a given set of external loads (e.g., Siev and Eidelman 1964; Argyris et al. 1974; Tabarrok and Qin 1992). Methods in this rationale can be viewed as simulating the physical hanging models using the finite element method. Drawbacks include the computationally expensive construction of the stiffness matrices, and the possibility to obtain compressive members in what should be a tension-only structure (Haber and Abel 1982). An alternative approach was later proposed that solves for the steady state of a dynamic equilibrium problem, which is equivalent to the equilibrium state of the static problem (Barnes 1977, 1988). This dynamic approach was later used in the design of axial-force-only particle-spring systems (Kilian and Ochsendorf 2006). Methods based on dynamic relaxation are typically faster than those based on stiffness matrices, but require additional parameters which may not have physical meaning, and may require tuning to ensure the stability and convergence of the solution (Nouri-Baranger 2004; Miki et al. 2014). Circa 1970, the design of the Munich Olympic Complex required form-finding capabilities beyond those offered by the available methods (Lewis 2003). The *Force Density Method* (FDM) was developed in response to this requirement: the form is obtained in a purely geometric manner by ensuring equilibrium of forces, but requiring assumptions on the members' force densities, defined as the force divided by the length of the member (Linkwitz and Schek 1971; Schek 1974). The computations involved in the FDM make it relatively inexpensive compared to stiffness-based methods, and hence it rose quickly in popularity due to the relatively scarce computational resources of the time. The method has been extended and modified numerous times to alleviate specific problems, or expand its capabilities (e.g., Haber and Abel 1982; Bletzinger and Ramm 1999; Nouri-Baranger 2004; Sánchez et al. 2007; Pauletti and Pimenta 2008). In addition to the aforementioned techniques, other works make use of structural optimization (Bletzinger and Ramm 1993, 2001; Bletzinger et al. 2005), or *graphic statics* (Block and Ochsendorf 2007; Block 2009; Thrall et al. 2012; Akbarzadeh et al. 2015), to name a few. None of these methods is free of issues, and therefore there is ongoing research to improve existing or develop new form-finding methods. The reader is referred to Lewis (2003) and Veenendaal and Block (2012) for a more thorough comparison of the most popular form-finding methods.

1.2 Review of form-finding by the force density method (FDM)

The force density method (FDM) by Linkwitz and Schek (1971) (in German) and Schek (1974) is a form-finding method for general cable network structures. In this method, a parameter called *force density* is defined as the ratio of the (signed) member force over the member length. Given the user-defined force densities and member connectivity, a fixed geometric stiffness matrix can be constructed, which relates the geometry (form), with the force equilibrium at each node. The solution of this system yields the nodal coordinates for which the geometry is under equilibrium for the given external loads. In the present work, an iterative scheme is introduced to cope with the design-dependent load calculation described in Section 2. It should be noted however, that this method does not consider the constitutive laws nor the compatibility equations. Thus, the resulting geometry is not dependent on the initial geometrical configuration of the network. The equations involved in the FDM are given in Appendix A for completeness.

2 Load derivation

In the following section, the loads in the $\{x, y, z\}$ directions for a node i are defined as $\mathbf{f}_i$. These nodal loads are built from three types of sources: loads applied directly at the nodes $\mathbf{f}_i^{\bullet}$, line loads on the edges $\mathbf{f}_i^{\diagup}$, and area loads from the polygonal panels $\mathbf{f}_i^{\square}$. The total load is therefore:

$$\mathbf{f}_i = \mathbf{f}_i^{\bullet} + \mathbf{f}_i^{\diagup} + \mathbf{f}_i^{\square} \quad \forall\, i = 1, 2 \ldots N_n \tag{1}$$

where N_n is the number of nodes in the network.

In the form-finding process, the nodal loads are dependent on the displacements: the load contributions coming from $\mathbf{f}_i^{\diagup}$ and $\mathbf{f}_i^{\square}$ are updated based on the (new) nodal locations. Thus, the algorithm iterates until some convergence criterion is met. In the case of the PEM and FDM methods, we use a displacement-based criterion:

$$\frac{\left|\mathbf{u}^{\text{new}} - \mathbf{u}^{\text{old}}\right|}{N_f} < \varepsilon \tag{2}$$

where $\mathbf{u}^{\text{new}}$ and $\mathbf{u}^{\text{old}}$ are the updated and previous nodal displacements, respectively, N_f is the number of degrees of freedom, and ε is a user-defined tolerance. Whereas in the GSM, there is a user-defined number of iterations. Nonetheless, for this last method, an automatic convergence criterion can be implemented based on variations of the interpolated surface.

2.1 Panel loads

The panel loads are resolved to their respective nodes using a tributary area distribution. The methodology can not only handle triangles and quadrangles, but any convex polygon[1]. The polygonal panels are triangulated from the center of mass (CM) as shown in Fig. 1a; which is calculated using a temporary triangulation from the average of the panel's nodal coordinates. It should be noted that this procedure will introduce error if the panels are significantly warped out-of-plane. Thus, it is assumed that the panel partition has a relatively small out-of-plane warping.

The area of the polygon's triangles are calculated sequentially: half of each triangle's area is assigned to the corresponding exterior node, as shown in Fig. 1a. This process is repeated for all load panels, and thus the tributary area associated with a node may receive contributions from multiple load panels (see Fig. 1b).

The panel load can itself be of three types: self-weight by unit area q, projected load $\mathbf{w}$ in the $\{x, y, z\}$ directions respectively, and an internal pressure p normal to each panel. A two-dimensional simplified illustration of these is shown in Fig. 2.

Thus, for a node i in the network, the loads in the $\{x, y, z\}$ direction due to panel loads are:

$$\mathbf{f}_i^{\square} = \sum_{\triangle} 0.5\left(\delta_{ij} + \delta_{ik}\right)\left(a_{jk}^{\triangle}\right)\left(q\hat{\mathbf{e}}_3 + \mathbf{w} : \hat{\mathbf{n}}_{jk}^{\triangle} + p\hat{\mathbf{n}}_{jk}^{\triangle}\right) \tag{3}$$

where $a_{jk}^{\triangle}$ is the area of a single triangle in the polygon's triangulation associated with the exterior nodes j and k (see Fig. 1a), δ_{ij} is the Kronecker delta (ensuring loads are only added to the exterior nodes in the triangle), q is the self-weight of the panel by unit area applied in the positive z direction (i.e. q is usually negative), $\hat{\mathbf{e}}_3$ is the unit vector in the positive z direction, $\mathbf{w}$ is the projected distributed load in the $\{x, y, z\}$ directions respectively, $\hat{\mathbf{n}}_{kj}^{\triangle}$ is the unit normal vector of a single triangle associated with the exterior nodes j and k, and p is the internal pressure load by unit area (positive outwards). For each triangle in the polygon's triangulation, we derive its area a_{ij} and unit normal vector $\hat{n}_{ij}$ by

$$\begin{aligned} \mathbf{n}_{ij}^{\triangle} &= \mathbf{v}_i \times \mathbf{v}_j \\ a_{ij}^{\triangle} &= 0.5\left|\mathbf{n}_{ij}^{\triangle}\right| \\ \hat{\mathbf{n}}_{ij}^{\triangle} &= \mathbf{n}_{ij}^{\triangle} / \left|\mathbf{n}_{ij}^{\triangle}\right| \end{aligned} \tag{4}$$

where $\mathbf{v}_i$ is the vector from the polygon's center of mass to node i (see Fig. 1a).

[1] Minor concavities can be handled, but are generally not advised since they may introduce structural instabilities in the node–bar network.

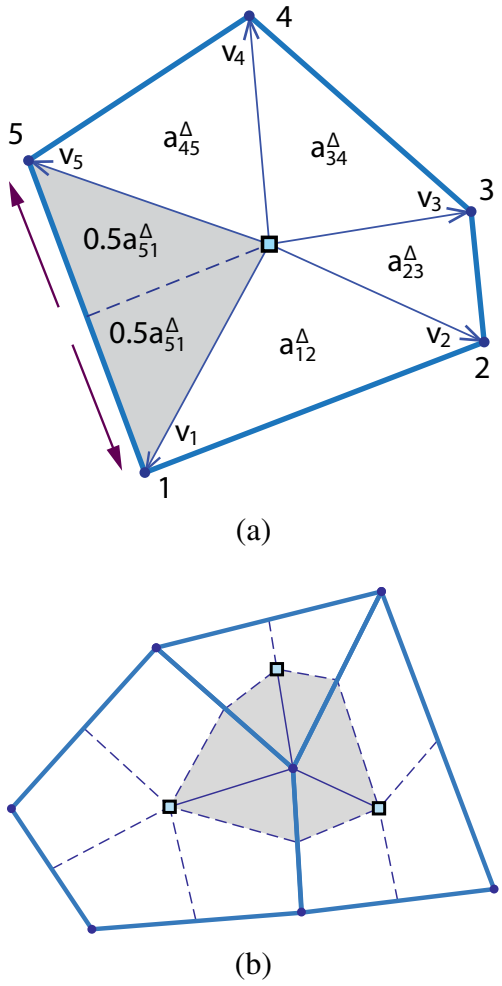

Fig. 1 Tributary area derivation: **a** A polygonal panel is triangulated from the center of mass. For each triangle, the area is calculated and then evenly assigned to the two adjacent nodes. Arrows indicate the nodes that the tributary area is assigned to; **b** Tributary area associated with a single node in the network

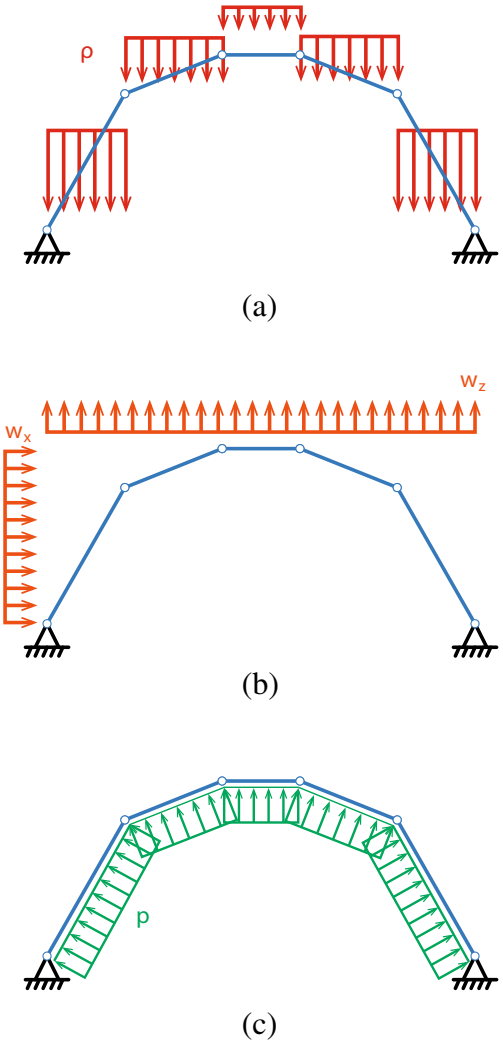

Fig. 2 Two-dimensional illustration for the 3 types of panel load: **a** Self-weight; **b** Projected load; **c** Internal pressure

2.2 Edge loads

The edge loads are calculated based on the length ℓ_{jk} and cross-sectional area a_{jk} of the bar between nodes j and k. Half of the bar's weight is assigned to each node. The implementation of projected loads in linear members is relatively simple; however, these loads are rare in practice, and are therefore not considered in this work. Thus, for a node i in the network, the nodal loads in the $\{x, y, z\}$ direction due to the edges are:

$$\mathbf{f}_i^{\diamond} = \sum_{\diamond} 0.5\left(\delta_{ij} + \delta_{ik}\right)\left(\ell_{jk} a_{jk}\right)\left(\gamma\, \hat{\mathbf{e}}_3\right) \tag{5}$$

where γ is the specific weight of the bars.

3 Form-finding by the potential energy method (PEM)

The *potential energy method* (PEM) finds the form in equilibrium by minimizing the total potential energy of the system, as its name suggests. This approach considers large deformations in the expression for the potential energy, where the designer can implicitly control the resulting form by manipulating the material properties and the initial nodal positions. The design is in an up-side-down configuration, which mimics the 3D hanging chain models used by Antoni Gaudí (Bergós and Llimargas 1999; Collins 1977; Martinell et al. 1975). The reciprocal relationship between the up-side-down tension-only structure and the standing compression-only structure under the same loading case is illustrated in Fig. 3, which is inspired by Zalewski and Allen (1997). To prevent members in undesired compression, the snap-through process is triggered by relaxing the stiffness of

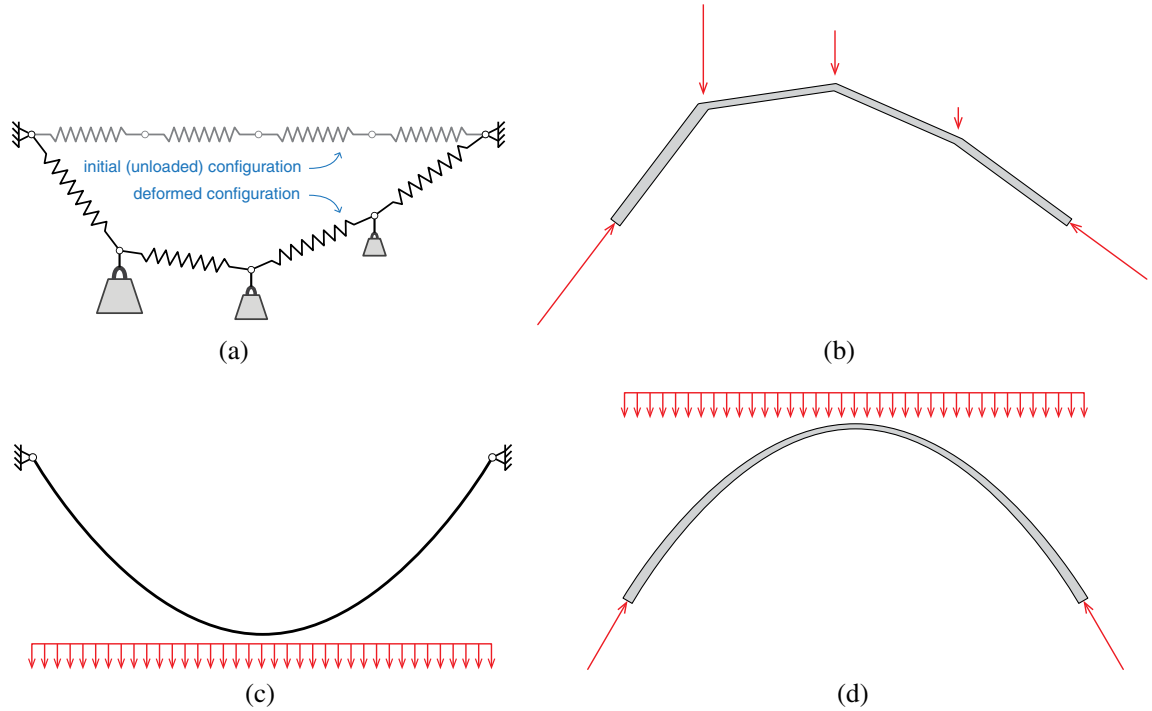

Fig. 3 A funicular in pure tension can be inverted vertically to obtain a compression-only funicular and vice-versa: **a** Tensile funicular form obtained by suspending three weights from springs or cables; **b** Compression-only funicular obtained from inverting the three-weight tensile form; **c** Deformed configuration for a cable in tension under a uniformly distributed load; **d** Compression-only quadratic arch obtained from inverting a cable under a uniformly distributed load

these members in compression (Jiang 2015). The following subsections elaborate on the details of the PEM.

3.1 Initial network generation

The first step for grid-shell form-finding with the PEM is to generate an initial network. This initial network is comprised of hinge nodes, bar members, boundary conditions, and (optional) load panels. Figure 4 illustrates how an initial network is generated for a small example. The nodes are defined by their 3-dimensional coordinates in space, with support boundary conditions added where appropriate. Bar members are defined by a pair of nodes with their ordering having no effect in the network definition. *Load panels* are defined by the numbering of their vertices: the panel has a positive normal *outwards* based on counter-clockwise ordering. This can define panel meshes such as the one shown in Fig. 4a. Load panels can have any number of sides and do not contribute to the structural behavior. Bar members can be automatically generated from the load panels if required, with differentiation of the inner and boundary members if necessary[2]. If the nodes at both ends of a bar are fixed, the bar is not considered in the form-finding process and is removed from the network. Using the automatic generation from load panels, a total of 12 bar members are defined as illustrated in Fig. 4b.

The method's goal is to find a suitable form in equilibrium under a single load case, where the members suffer no bending moment or shear force (other than those caused by self-weight between nodes). All bar members will be subject to axial loads only with the following assumptions:

1. All bar members are hinge-connected;
2. Loads are only applied at the nodes.

3.2 Formulation of the potential energy method

The total potential energy PE is defined as the sum of member strain energy minus the work done by the external loads. Thus, the minimization statement is:

$$\min_{\mathbf{u}} \quad \text{PE} = \sum_{i=1}^{N_b} \frac{1}{2} \widetilde{k}_i \left(\Delta \ell_i\right)^2 - \{\mathbf{f}(\mathbf{u})\}^T \mathbf{u} \tag{6}$$

where $\widetilde{k}_i$ is a reduced and relatively low axial stiffness associated with the i-th member for the form-finding process only, $\Delta \ell_i$ the i-th member's change in length, $\mathbf{f}$ is the nodal load vector (dependent on the displacements) calculated as per Section 2 of the present manuscript, and $\mathbf{u}$ is the nodal displacement vector. The unconstrained minimization problem is solved by a quasi-Newton algorithm with the

[2]Each inner member forms the edge of 2 load panels while each boundary members forms the edge of 1 load panel.

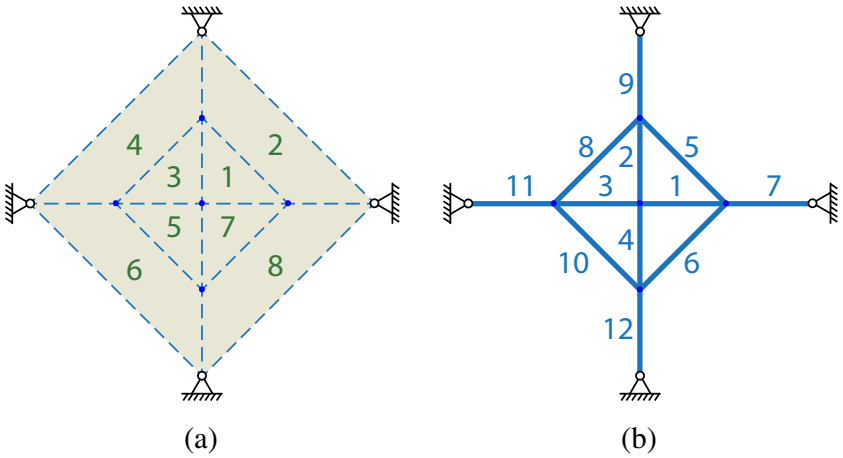

Fig. 4 Initial network generation for a simple example: **a** Eight load panels enclosed by dashed lines; **b** Twelve active bar members between hinged nodes

BFGS Hessian updating scheme. Note that **f** is dependent on the displacements, which introduces a nonlinearity into the problem. Thus, we iterate until the form is in equilibrium for the loads under the updated configuration (within a small error tolerance).

The final grid-shell form is determined by deformation of the initial configuration, which means that the resulting form is dependent on the initial domain geometry. While this can be seen as a drawback of the current method, it can be used as an additional degree-of-freedom to tune the resulting shape (in addition to the reduced member stiffnesses $\widetilde{k_i}$).

3.3 Snap-through triggering

A network of pin-connected bars may have more than one equilibrium configuration, with the resulting shape determined by the loading history. Under certain conditions, the PEM may converge to a solution with one or more members in compression. An illustrative example in Fig. 5 shows an equilibrium configuration with an undesirable kink composed of members in compression. The configuration indicates a local minimum of the potential energy. These members in compression are likely to have another valid configuration in tension, which can be attained after undergoing a *snap-through*. Figure 6 illustrates the concept of these two configurations separated by a snap-through. Consider a 2-bar truss system loaded vertically downwards at the center node by a force p, as shown in Fig. 6a. If the load is large enough (force p_A) to load beyond the snap-through multi-stable region, the only equilibrium

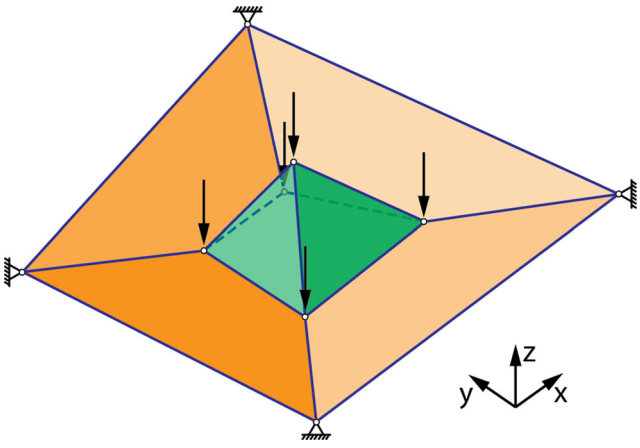

Fig. 5 An example of a possible equilibrium configuration with members in compression. These members comprise a kink, which may be avoided if a snap-through action takes place. Arrows on nodes denote nodal loads

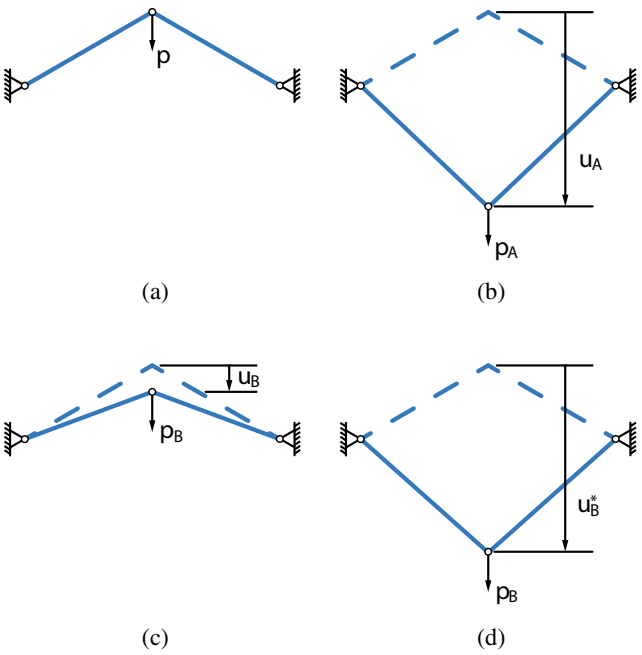

Fig. 6 A two-bar truss system loaded at the center with a snap-through behavior: **a** Unloaded configuration; **b** Case A—equilibrium configuration for a large load; **c** Case B—equilibrium configuration for a small load, where bars are in compression; **d** Case B—equilibrium configuration for a small load, where bars are in tension

configuration is in tension (Case A) and is shown in Fig. 6b. However, if the load is small (force p_B), there may be two possible equilibrium configurations that are stable (Case B). Based on the initial configuration and assuming a relatively slow and monotonic loading history, the equilibrium configuration is reached after a small displacement u_B with both members in compression, as shown in Fig. 6c. The second stable configuration, shown in Fig. 6d, has both members in tension: the node has snapped-through downwards and the displacement $u_B^\star$ is large compared to u_B. In the context of form-finding, the configuration in Fig. 6d is preferred, since this will result in a compression-only grid-shell once the result is inverted (or flipped) up-side-down: a feature usually sought in grid-shell structures.

The snap-through load-displacement behavior for this two-bar problem is illustrated in Fig. 7. Because the load history and initial configuration determine the final deformed shape of the loaded structure (Leon et al. 2011), the computational algorithm by which the structure is loaded and solved will have impact on the solution. Starting from the configuration shown in Fig. 6a: for Case A the solution is unique (p_A, u_A), although depending on the algorithm used, the load history or path might not be correct; in Case B however, the stable solution $\left(p_B, u_B^\star\right)$ is reached before the preferred configuration at (p_B, u_B). To cope with the situation, a snap-through relaxation procedure is implemented. If a member is found in a state of compression, its stiffness will be reduced to a relatively small value (e.g. 1% of the original value), such that the snap-through condition is artificially triggered. Later in the solution iterations, if said member returns to a state of tension, its original stiffness is restored. Thus, in the context of the two-bar problem shown in Fig. 6, for Case B the equilibrium configuration will likely be the preferred tension-only (p_B, u_B), as illustrated in Fig. 7.

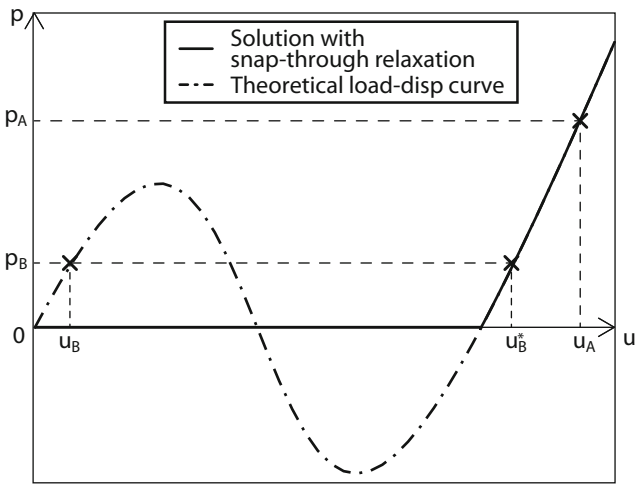

Fig. 7 The load-displacement plot for the two-bar system. The true load-displacement curve and the one using snap-through relaxation, coincide in the tension-only region but not on the compression regime

3.4 Member sizing

The member cross-sectional areas are designed such that the members are all fully-stressed. Coelho et al. (2014) document several experiences of grid-shell form-finding using commercial software and introduce an additional member sizing step after the final form is found (Coelho et al. 2014). The member sizing approach in the present work considers large displacements in the analysis, which is performed using the minimum potential energy approach. Based on the analysis result, the members are sized using the *stress ratio method* (Gallagher and Zienkiewicz 1973; Barnes et al. 1977). The stress ratio method can consider different limits in tension and compression, however due to the snap-through relaxation described in Section 3.3, only the tension limit is used by the algorithm (compression once the result is flipped up-side-down). The stress ratio method is an iterative procedure which can include considerations for buckling or other criteria. Common steel section families have their moment of inertias proportional to their cross-sectional areas (Baker 1992). Thus, the inclusion of elastic buckling in the stress limit is straightforward provided that a section family is chosen. However, for the sake of simplicity and generality of the present work, this limit value is assumed constant (i.e. no buckling criterion is used).

Given a set of member cross-sectional areas, the equilibrium state is solved by the PEM:

$$\min_{\mathbf{u}} \quad \text{PE} = \sum_{i=1}^{N_b} \frac{1}{2} k_i \left(\Delta \ell_i\right)^2 - \mathbf{f}^T \mathbf{u} \tag{7}$$

where the stiffness of the i-th member is defined as

$$k_i = \frac{E_i a_i}{\ell_i} \tag{8}$$

in which E_i is the material Young's modulus, a_i is the cross-sectional area and ℓ_i is the member length.

Note that k_i is the (real) member stiffness (i.e. $k_i \gg \widetilde{k}_i$), and, assuming small displacements, the load does not depend on the displacements. The form-finding and member sizing formulations presented ((6) and (7) respectively), bear many similarities with the key differences being:

1. In the member sizing, the member stiffness k_i is calculated by (8); whereas $\widetilde{k}_i$ is user-defined and comparatively low.
2. In the member sizing, the nodal load vector $\mathbf{f}$ is assumed to be constant; whereas in the form-finding (6), $\mathbf{f}$ is dependent on the form. In the member sizing stage, we

assume that the cross-section change introduces a relatively small change in the overall form, resulting in negligible changes in the loads[3].

The cross-sectional member areas are then updated by the *stress ratio method* (Gallagher and Zienkiewicz 1973; Barnes et al. 1977), where $\sigma_{adm,i}$ is the limit admissible stress[4] for the i-th member:

$$a_i^{k+1} = a_i^k \left(\frac{\sigma_i^k}{\sigma_{adm,i}} \right)^{\eta} \tag{9}$$

where a_i^k and a_i^{k+1} are the cross-sectional areas of the i-th member in the current and next iteration respectively. The *stress ratio* is defined as the ratio of the current member stress σ_i^k over the member's admissible stress $\sigma_{adm,i}$, and is used as a factor to update the cross-sections. The parameter η is a numerical damper $0 < \eta \leq 1$ that improves the convergence and stability of the method. Based on experience, good results are expected for η in the range of $[1/2, 1/3]$, with lower values recommended in the event that buckling limits are considered (buckling introduces an additional design nonlinearity).

During some design trials, we observe that the member sizing may result in a design that is almost fully-stressed but with some grid members with a stress ratio less than 1. As iterations proceed, these non-fully-stressed grid members should vanish with negligible cross-section areas. It should be noted, however, that the stresses of these *vanishing* members can be non-zero and still be determined without a cross-section: stresses can be calculated with displacements and constitutive relations only (case of a singular topology, refer to Rozvany (2001)).

3.5 Group member sizing

For cost and constructibility purposes, the design may be restricted to a reduced number of distinct cross-sectional areas. This can be achieved by a group member sizing, where bar members in the same user-defined group will have identical cross-sectional areas. All members within a group g will have the same cross-section a_g throughout the design process (including the initial guess). The stress ratio updating scheme is modified to be

$$a_g^{k+1} = a_g^k \left[\max_{j \in \mathbb{G}_g} \left(\frac{\sigma_j^k}{\sigma_{adm,g}} \right) \right]^{\eta} \tag{10}$$

where $\mathbb{G}_g$ is a user-defined group of members with equal cross-sectional area a_g, and admissible tension limit $\sigma_{adm,g}$, for all $g = \{1, 2, 3 \ldots\}$ number of groups. This updating scheme will not result in a fully-stressed design; instead each group should have at least one fully-stressed member (assuming the solution is not degenerate (Rozvany 2001)).

3.6 Summary of form-finding by the PEM

The processes of form-finding by PEM and member sizing are summarized with flowcharts in Fig. 8. Note that as the form-finding and member sizing are separate processes, the form and load input for member sizing is not restricted to the PEM results.

4 Form-finding by the ground structure method (GSM)

The *ground structure method* (GSM) is a topology optimization technique developed for obtaining the optimal geometry, connectivity, and cross-sections of pin-jointed frameworks or trusses (Dorn et al. 1964). This method has seen extensive use as an aid in the derivation of closed-form analytical solutions for optimal structures (Lewiński et al. 1994; Rozvany et al. 1997; Pichugin et al. 2012; Lewiński et al. 2013; Sokół and Rozvany 2013; Rozvany and Sokół 2013 Sokół 2011, 2014). The power of the method lies in its ability to formulate the optimization statement as a linear programming[5] problem (Hemp 1973). The linear programming problem can be solved very efficiently using the interior-point method family of linear program solvers (Karmarkar 1984; Wright 2004). The method requires an initial highly-redundant and interconnected truss network, the *ground structure*, from which the *best possible solution* is extracted, with this being an approximation of the theoretical optimum. Since the solution will only contain members in the original ground structure, this ground structure can be tailored (or specially generated) to meet the design requirements or geometric restrictions. The method is only limited by the user's ability to generate this ground structure. Recently, a methodology was introduced to generate ground structures in any two-dimensional domain, including concavities and holes, based on graph theory and collision detection (Zegard and Paulino 2014). This methodology was later extended to three-dimensional space (Zegard 2014; Zegard and Paulino 2015), and thus serves as the foundation for this section.

[3] The load could depend on the displacements or the cross-sections, but because the displacements are small, they are assumed constant for the sake of simplicity.

[4] Considering the material's yield limit, and optionally including considerations for buckling or other criteria.

[5] There are two common versions of the GSM: one based on the *plastic formulation*, and one based on the *elastic formulation*. Only the *plastic formulation* can be formulated as a linear programming problem. The *elastic formulation* (Bendsøe et al. 1994; Christensen and Klarbring 2009; Ramos and Paulino 2015), despite being computationally more expensive, considers compatibility and can include material and geometric non-linearities to name a few features. The present work uses the *plastic formulation* in the form-finding process.

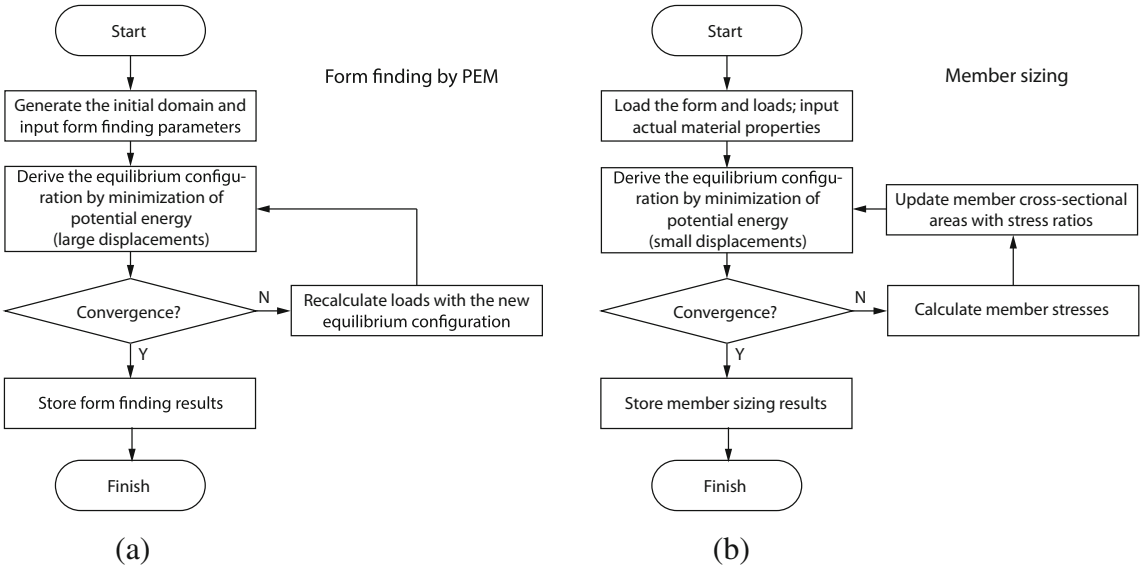

Fig. 8 Process of form-finding by the PEM and member sizing: **a** Flowchart for form-finding by the PEM; **b** Flowchart for member sizing

The optimization formulation for the (plastic version of the) GSM is:

$$\begin{aligned} \min_{\mathbf{s}^+,\mathbf{s}^-} \quad & \left\{ \boldsymbol{\ell}^T \kappa \, \boldsymbol{\ell}^T \right\} \left\{ \begin{array}{c} \mathbf{s}^+ \\ \mathbf{s}^- \end{array} \right\} = \sigma_T \, V \\ \text{s.t.} \quad & \left[\mathbf{B}^T \; -\mathbf{B}^T \right] \left\{ \begin{array}{c} \mathbf{s}^+ \\ \mathbf{s}^- \end{array} \right\} = \mathbf{f} \\ & \mathbf{s}^+, \mathbf{s}^- \geq 0 \end{aligned} \tag{11}$$

where s_i^+ and s_i^- are (positive) slack variables associated with the tension and compression force of the i-th member respectively, $\kappa = \sigma_T/\sigma_C$ is the ratio of the tension to compression stress limits, $\boldsymbol{\ell}$ is the vector of member lengths, and V is the volume of the resulting structure. The matrix $\mathbf{B}^T$ is the nodal equilibrium matrix built from the directional cosines of the members, and $\mathbf{f}$ is the nodal force vector, both excluding the components associated with supports. The cross-section of the i-th member is $a_i = s_i^+/\sigma_T + s_i^-/\sigma_C$, and the respective force is $n_i = s_i^+ - s_i^-$. The solution to this problem assumes the design is *fully stressed*, which is valid for problems with a single load case. For additional details on the assumptions and derivations leading to (11) the reader is referred to Hemp (1973) and Zegard and Paulino (2014).

4.1 Formulation with transmissible loads

The GSM finds the optimal structure (within the ground structure) given the nodal loads and supports. This poses a difficulty for grid-shell form-finding: since the grid-shell geometry is not known a priori, the points of application of the loads are unknown. Rozvany and Wang (1983) and Wang and Rozvany (1983) use the concept of *transmissible loads*: the load is applied to *fictitious* nodes connected by *virtual* members to the real structure. These members are essentially *free* and allow the load to position itself optimally. It may be incorrectly assumed that this is equivalent to making the vertical members in the ground structure *free*, which in the context of (11) translates into artificially assigning a zero member length to verticals: the (ideally) unique solution will be repeated vertically multiple times because the optimal lies in an edge or facet of the feasible domain (infinite solutions). As a consequence, the numerical result will vary with the linear program solver used: for the benchmark problem in Fig. 9a, the solution using the modified version of LIPSOL in MATLAB® (Zhang 1996a, b) is shown in Fig. 9b, where the repetition artifact of this flawed approach is clear.

The approach of *transmissible loads* using virtual bars has also been applied to continuum optimization (Fuchs and Moses 2000; Chiandussi et al. 2009; Yang et al. 2005). Instead of *virtual* vertical members, the *transmissible loads* can be analogously implemented by extending the problem in (11) to include the vertical loads as variables, and adding equations to maintain equilibrium (Gilbert et al. 2005; Darwich et al. 2010). The present work considers a generalization of this extended formulation, allowing for any number, direction and magnitude of the transmissible loads. This approach is combined with an adaptive and unstructured discretization of the domain used to generate the ground structure (Zegard and Paulino 2015). The solution in Fig. 9c is the result of this proposed method,

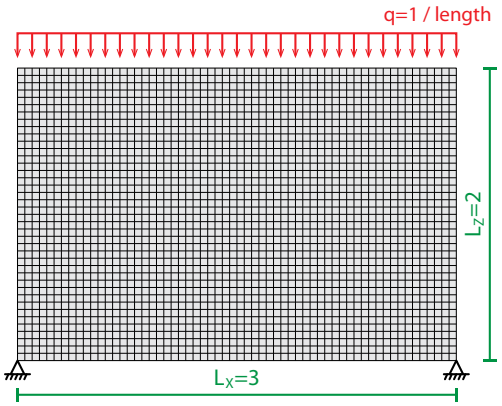

(a)

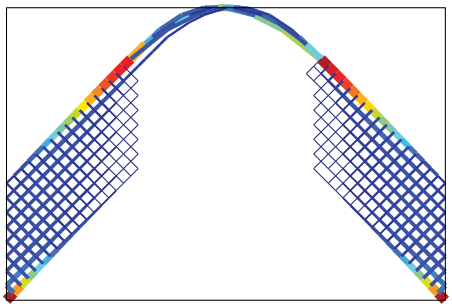

(b)

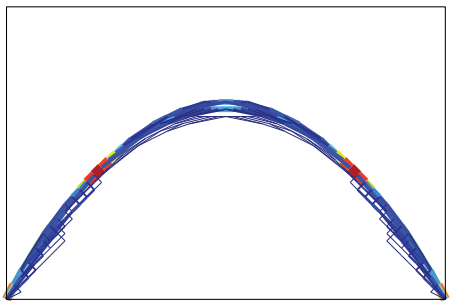

(c)

Fig. 9 Regular and orthogonal simple mesh to illustrate the transmissible loads in the GSM: **a** Base mesh of 60×40 elements used in the ground structure generation; **b** Assigning *zero* length to the vertical members leads to an (incorrect) degenerate solution that is repeated vertically; **c** Solution obtained using the augmented GSM with transmissible loads, with equal limits in tension and compression (i.e. $\kappa = \sigma_T/\sigma_C = 1$)

where the *spokes* radiating or branching from the supports are indeed part of the optimal solution for the case of equal limits in tension and compression (Darwich et al. 2010; Tyas et al. 2010). Conversely, the solution for a compression-only arch under a constant distributed load is a parabolic arch (Rozvany and Wang 1983), which will be used to verify the proposed method.

The unknown vertical loads are integrated as variables in the linear program by augmenting the system in (11). This is done by splitting the equations associated with the vertical

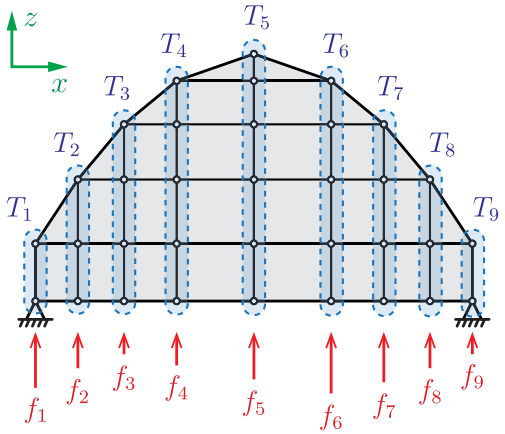

Fig. 10 Simple domain discretization with 9 transfer groups. Transfer groups can have different numbers of nodes

loads (z direction, as in Fig. 10) and horizontal in-plane loads (x and y direction):

$$\begin{aligned} \min_{\mathbf{s}^+,\mathbf{s}^-} \quad & \left\{ \boldsymbol{\ell}^T \kappa \, \boldsymbol{\ell}^T \right\} \left\{ \begin{array}{c} \mathbf{s}^+ \\ \mathbf{s}^- \end{array} \right\} = \sigma_T \, V \\ \text{s.t.} \quad & \left[\begin{array}{cc} \mathbf{B}_{xy}^T & -\mathbf{B}_{xy}^T \\ \hline \mathbf{B}_z^T & -\mathbf{B}_z^T \end{array} \right] \left\{ \begin{array}{c} \mathbf{s}^+ \\ \mathbf{s}^- \end{array} \right\} = \left\{ \begin{array}{c} \mathbf{f}_{xy} \\ \mathbf{f}_z \end{array} \right\} \\ & \mathbf{s}^+, \mathbf{s}^- \geq 0 \end{aligned} \tag{12}$$

where $\mathbf{f}_{xy}$ are the nodal loads associated with the x and y coordinates, and $\mathbf{f}_z$ are the vertical nodal loads. The subscripts xy denote an aggregation of terms associated with the x and y coordinates, i.e.:

$$\mathbf{B}_{xy}^T = \left\{ \begin{array}{c} \mathbf{B}_x^T \\ \mathbf{B}_y^T \end{array} \right\} \quad , \quad \mathbf{f}_{xy} = \left\{ \begin{array}{c} \mathbf{f}_x \\ \mathbf{f}_y \end{array} \right\} \tag{13}$$

The vertical loads $\mathbf{f}_z$ are allowed to transfer (or move) vertically to optimally position themselves within a *transfer group*: a transfer group T_i is defined by all nodes sharing the same x and y coordinates (within some small tolerance), as shown in Fig. 10. It should be noted that there is no order or structured requirement; i.e. the *transfer groups* can have different size and are automatically generated. The total load $(f_v)_i$ associated with the i-th transfer group T_i will be distributed among the nodes of the group, thus:

$$(f_v)_i = \sum_{j \in T_i} (f_z)_j \tag{14}$$

with $(f_v)_i = 0$ if any vertical (z direction) degree-of-freedom in group T_i is supported. If the (vertical) load can position itself anywhere in the transfer group, the existence of a support will draw all the loads to itself.

The nodal vertical loads $\mathbf{f}_z$ are split into a (positive) magnitude $\mathbf{f}_z^\star$ and direction $\boldsymbol{\beta}$, therefore:

$$\mathbf{f}_z = \boldsymbol{\beta} : \mathbf{f}_z^\star \tag{15}$$

This splitting is convenient since standard linear programs require all variables to be positive, and the goal is to make $\mathbf{f}_z$ a variable in the optimization statement. Thus, the nodal equilibrium in the z direction becomes:

$$\mathbf{B}_z^T \left(\mathbf{s}^+ - \mathbf{s}^-\right) - \text{diag}\left(\boldsymbol{\beta}\right) \mathbf{f}_z^\star = \mathbf{0}\,, \tag{16}$$

with the load direction vector $\boldsymbol{\beta}$ defined as:

$$\beta_i = \begin{cases} 1 & \text{if } i \in T_j \text{ and } f_j \geq 0 \\ -1 & \text{if } i \in T_j \text{ and } f_j < 0 \end{cases} \tag{17}$$

A rectangular matrix $\mathbf{A}$ indicates the correspondence of a node to a transfer group:

$$A_{pq} = \begin{cases} 1 & \text{if } q \in T_p \\ 0 & \text{otherwise} \end{cases} \tag{18}$$

with an explicit relationship between the correspondence matrix $\mathbf{A}$ and the load direction vector: $\boldsymbol{\beta} = \mathbf{A}^T \text{sgn}^\star\left(\mathbf{f}_v\right)$, with $\text{sgn}^\star(\cdot)$ being the *sign* operator reserving that $\text{sgn}^\star(0) = 1$. It is assumed that every node belongs to a single transfer group T_i, and that all nodes belong to a transfer group (even if the group contains a single node). By naming $\mathbf{f}_v$ the vector of vertical transfer loads associated with each transfer group, the augmented ground structure formulation is:

$$\begin{aligned} \min_{\mathbf{s}^+,\mathbf{s}^-,\mathbf{f}_z} \quad & \left\{\boldsymbol{\ell}^T \;\kappa\,\boldsymbol{\ell}^T \;\mathbf{0}^T\right\} \begin{Bmatrix} \mathbf{s}^+ \\ \mathbf{s}^- \\ \mathbf{f}_z \end{Bmatrix} = \sigma_T\, V \\ \text{s.t.} \quad & \left[\begin{array}{cc|c} \mathbf{B}_{xy}^T & -\mathbf{B}_{xy}^T & \mathbf{0} \\ \hline \mathbf{B}_z^T & -\mathbf{B}_z^T & -\text{diag}\left(\boldsymbol{\beta}\right) \\ \hline \mathbf{0} & \mathbf{0} & \mathbf{A} \end{array}\right] \left\{\begin{array}{c} \mathbf{s}^+ \\ \mathbf{s}^- \\ \hline \mathbf{f}_z^\star \end{array}\right\} = \left\{\begin{array}{c} \mathbf{f}_{xy} \\ \hline \mathbf{0} \\ \hline |\mathbf{f}_v| \end{array}\right\} \\ & \mathbf{s}^+, \mathbf{s}^-, \mathbf{f}_z \geq 0 \end{aligned} \tag{19}$$

where the relation $\mathbf{A}\mathbf{f}_z^\star = |\mathbf{f}_v|$ is enforcing the vertical loads to add to the specified external vertical loads (14). Equation (19) is the main optimization formulation adopted in this work.

4.2 Surface interpolation and refinement

The location of the grid-shell surface is interpolated based on the point of application of the transmissible load. For each transfer group T_j, the vertical location of the grid-shell surface $\bar{z}_j$ is the weighted average of the node vertical position z_i, weighted by the fraction of transmissible load in it $\left(f_z^\star\right)_i$:

$$\bar{z}_j = \frac{\sum_{i \in T_j} (z_i) \left(f_z^\star\right)_i}{\sum_{i \in T_j} \left(f_z^\star\right)_i} = \frac{\sum_{i \in T_j} (z_i) \left(f_z^\star\right)_i}{|f_v|_j} \tag{20}$$

with $|f_v|_j$ being the magnitude of load applied in the j-th transfer group. In the event that no vertical loads are assigned to a transfer group, an equivalent procedure can be done using the relative cross-sections of members connecting to each node within a group.

It has been shown that the tension region spokes in the arch solution in Fig. 9c result in a better (lighter or less-compliant) structure than a compression-only arch (Darwich et al. 2010; Tyas et al. 2010). In the present work however, the interest is in compression-only solutions; which are also known as *Prager structures* (Rozvany and Prager 1979; Rozvany et al. 1982). The *spokes* radiating or branching from the supports in Fig. 9c constitute a compression-tension orthogonal field that will bias the surface interpolation towards a *shallow* configuration. The compression-only solutions can be filtered by reducing the tension to compression limit ratio κ in (19). It has been proven that for a two-dimensional arch, such as the benchmark problem in Fig. 9, a tension to compression limit ratio $\kappa = \sigma_T/\sigma_C < 1/3$ is sufficient to yield a compression-only solution (Darwich et al. 2010). In the three-dimensional case, and to cover a wide range of geometries and load configurations, ideally $\kappa \to 0$ to obtain compression-only solutions. However, a value of $\kappa = 0.01 > 0$ is used for numerical stability while still rendering *close-to* compression-only solutions: problems with overhanging awnings or cantilevers require a tension region, thus $\kappa > 0$ allows the algorithm to find a solution in those cases (though severely punishing the tension region).

The solution with $\kappa = 0.01$ for the benchmark problem in Fig. 9 is shown in Fig. 11a; with its interpolated

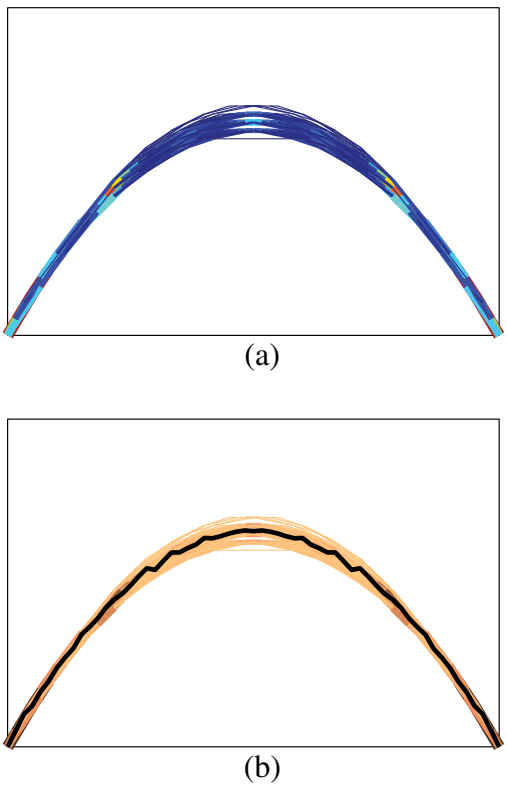

Fig. 11 Ground structure solution for the compression-only single arch: **a** Solution obtained using $\kappa = 0.01$ for the problem in Fig. 9a; **b** Surface interpolation obtained from (20)

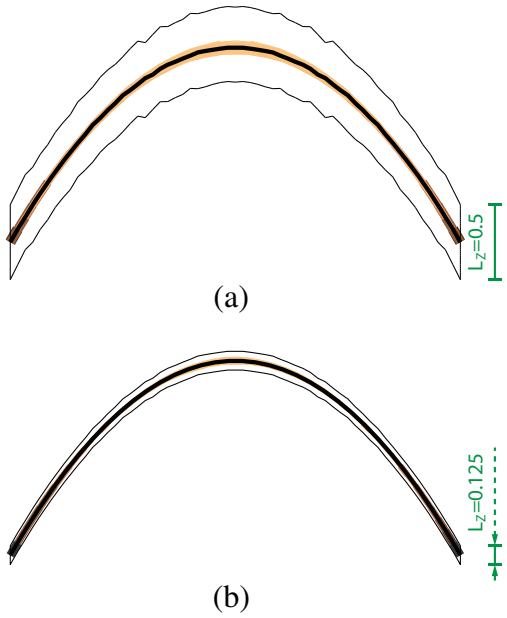

Fig. 12 Refinement of the domain for the problem in Fig. 9a: **a** First refinement. Surface is extruded in both directions for a total height of 0.5; **b** Second refinement. Surface is extruded in both directions for a total height of 0.125

surface shown in Fig. 11b. This interpolated surface is reasonably smooth, despite the coarseness of the domain partition and having a large portion of the ground structure outside the scope of the optimal arch (hence a large computational overhead). This interpolated surface is used to refine the discretization used in the ground structure generation by shrinking the domain, thus achieving better solutions. Figure 12a shows the result after shrinking the domain to 1/4 of the initial vertical span, based on the interpolated surface in 11(b): the supports are centered on the mesh, and the collinear tolerance[6] is reduced by 5% (initially $ColTol_0 = 0.999999$, thus $ColTol_1 = 1 - 0.05\,(1 - ColTol_0) = 0.99999995$). The result shown in Fig. 12b is obtained after repeating the process once more (again reducing the vertical span by 1/4 and the collinear tolerance by 5%).

The quality of the results and the efficacy of the refinement can be evaluated with help of the analytical solution: the summary of the results is displayed in Table 1. The GSM makes use of discrete nodal locations, and thus the surface interpolation can over- or under-estimate the height of the arch depending on the partition. However, the optimal volume will converge to the optimal volume from above as the solution improves.

In the three-dimensional space, the geometry (form-finding) of the grid-shell is determined by the surface interpolation procedure. The ground structure solution associated with it provides information on the optimal load-path

[6]Refer to Zegard and Paulino (2014) for details on the effect of the collinear tolerance on the ground structure generation process.

Table 1 Convergence and error of the arch height and volume with refinement for the problem in Fig. 9a

Case	Arch height	Volume V
Analytical	$\frac{\sqrt{3}L_x}{4} = 1.2990$	$\frac{4qL_x^2}{4\sqrt{3}\sigma_C} = 5.1962$
Orthogonal	1.3209	5.2200
grid	$error = 1.68\%$	$error = 0.46\%$
1^{st}	1.2962	5.2010
refinement	$error = -0.22\%$	$error = 0.09\%$
2^{nd}	1.2964	5.1962
refinement	$error = -0.20\%$	$error = 0.01\%$

of the forces in the optimized grid-shell geometry, which can be used to guide the optimal layout of the members in the grid-shell. In addition, previous work has also focused on the automatic layout of the members for a given grid-shell geometry (Richardson et al. 2013).

The method of transmissible loads using the ground structure generation framework from Zegard and Paulino (2015) was here exemplified with a two-dimensional example. While this section dealt with a known two-dimensional problem and a design-independent load, the power of the proposed method lies in its extension to three-dimensional space, and the capability of addressing (almost) any domain shape. The inclusion of self-weight, and design-dependent loads can be readily applied, and is described in Section 2. This is a remarkable property of the present GSM because in the case of a continuum density-based method, special procedures are needed to handle design-dependent loads (Bendsøe and Sigmund 2003).

5 Numerical examples

The three form-finding methods mentioned above are implemented and tested with three numerical examples. The examples include a quadratic synclastic dome, a polygonally tessellated pavilion and a doubly-curved *bowtie* surface.

- Quadratic synclastic dome: the simplicity of this problem allows for easy comparison and visual evaluation of the various results obtained with each method.
- Polygonally tessellated pavilion: this problem highlights the ability of the methods to address grid-shells with unstructured polygonal load panels with the possibility of holes and concavities.
- Doubly-curved bowtie surface: the capability to handle non-flat curved boundaries and to yield compression-only results are showcased with this example.

The units used are kilonewton (kN) for forces and meters (m) for length unless otherwise specified.

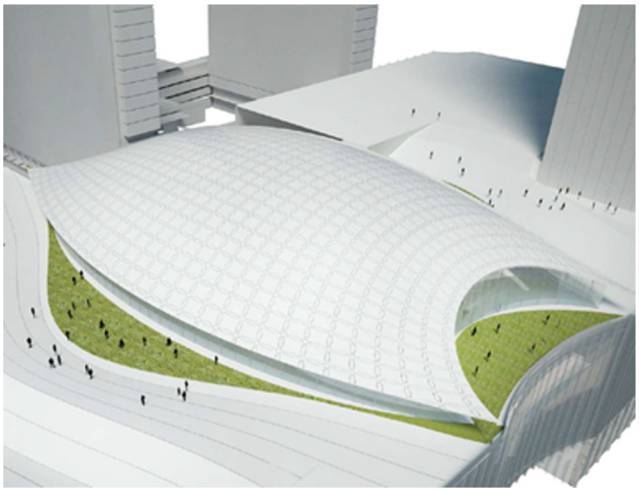

Fig. 13 Quadratic synclastic dome: rendering of the design competition used as inspiration for the design (image courtesy of SOM LLP)

5.1 Quadratic synclastic dome

This example addresses the form-finding of a synclastic dome with quadratic edges in the XY plane, which is illustrated in Figs. 13, 14, 15, 16, 17, 18, 19, 20 and 21. This problem is inspired by a competition design of Skidmore, Owings & Merrill LLP (SOM LLP) (see Fig. 13). The original design was obtained using a *heavy soap film*-inspired approach based on isogeometric continuum shell optimization. This approach considers a different treatment of the supports, with their geometry being part of the optimization process. The reader is referred to Mitchell (2013) for details on the procedure used to obtain the result in Fig. 13.

The grid-shell is meant to provide cover for a 2808 m^2 footprint. The edges are both quadratic in plane, with the longer edge convex outwards, and the shorter edges concave inwards as shown in Fig. 14. The longer edges are fixed to the ground level, while the opposite edges are open. Requirements of the design include:

- The opening should be no less than 5 m high;
- The apex height should be approximately 12 m.

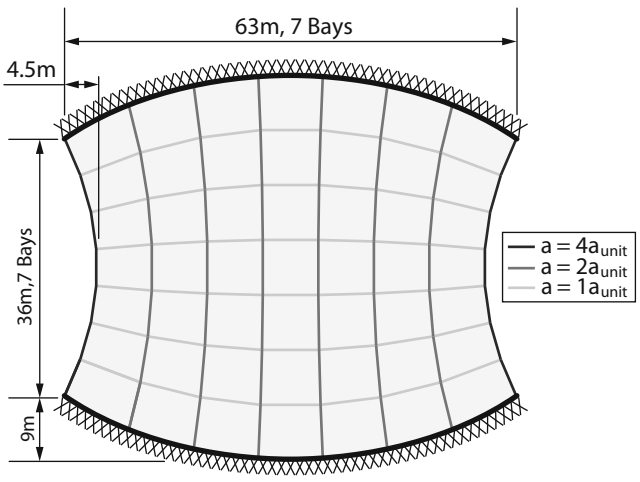

Fig. 14 Quadratic synclastic dome: footprint, panel mesh, boundary conditions, and the prescribed cross-sectional areas used in the PEM. The value of a_{unit} is 5, 000 mm^2 in the PEM-based form-finding stage

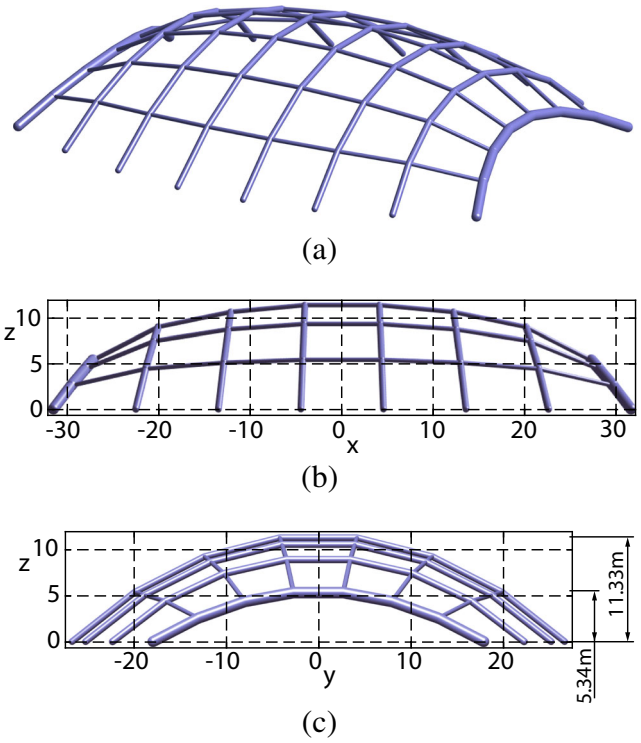

Fig. 15 Quadratic synclastic dome: form-finding result by the PEM. **a** Isometric view; **b** Front view; **c** Side view

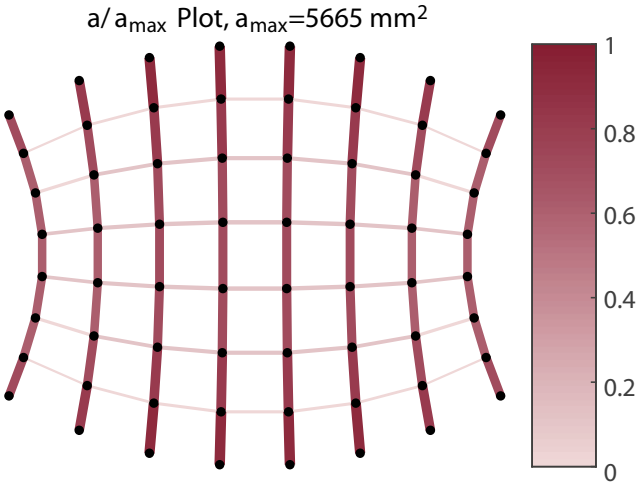

Fig. 16 Quadratic synclastic dome: area-ratio plot showing the ratio of the members' cross-sectional area over the maximum value in the structure. Both the line width and color-scale in the plot are correlated with the area-ratio.The maximum cross-sectional area a_{max} = 5, 665 mm^2

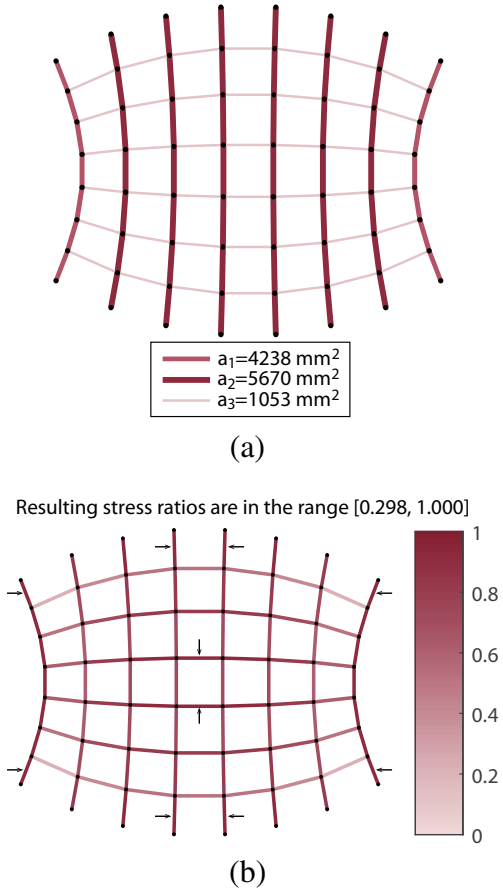

Fig. 17 Quadratic synclastic dome: group member sizing results. **a** Resulting cross-sectional areas for the three groups; **b** Stress ratio plot shows that each group has at least one fully-stressed member, as indicated by an arrow

5.1.1 PEM solution

The design domain is discretized into the structured network with 64 nodes, 49 load panels, and 98 bars (edges) as shown in Fig. 14. The system is loaded by its panels, considering a self-weight load of 4.5 kN/m^2 and an upward wind suction load of 0.5 kN/m^2. The member stiffnesses are determined by $\widetilde{k}_i = E_i a_i / \ell_i$, in which E is assumed to be 1 GPa for all members, and ℓ_i is the original length of the i-th member in the initial configuration (i.e. $z = 0$, $\forall \mathbf{x} = \{x, y, z\}$). The cross-sectional areas are shown in Fig. 14, where a_{unit} equals $5,000\,\text{mm}^2$. These fictitious cross-sections are tuned to yield the desired geometric requirements (opening height > 5 m, and apex height of ≈ 12 m).

The isometric, front, and side view of the form-finding results by PEM are shown in Fig. 15a, b and c, respectively. It can be observed from Fig. 15c that the openings are 5.34 m in height, with an apex height of 11.33 m, which conforms with the design requirements.

Member sizing is conducted after the form-finding stage using the stress ratio method with a numerical damping of $\eta = 0.5$. The design material is assumed to be A500 Gr. B carbon steel, with a Young's modulus of 200 GPa, and an admissible stress of 315 MPa. The admissible stress reduction factor is 0.9 against yielding. The critical load combination of 1.2 times the dead load and 1.0 times the wind load is considered, with these loads inherited from the form-finding stage. Starting from a uniform initial guess of $5,000\,\text{mm}^2$, the a_i values converge to those shown in Fig. 16 after 28 iterations. The maximum cross-sectional area is $5,665\,\text{mm}^2$, with all members reaching a stress ratio equal to 1.0 (within a tolerance of 0.0005).

Group member sizing is conducted for comparison. The members are divided into 3 groups as shown in Fig. 17a. Starting with an initial guess of $a_g = 5,000\,\text{mm}^2$ for all groups, the cross-sectional areas converge to $a_1 = 4,238\,\text{mm}^2$, $a_2 = 5,670\,\text{mm}^2$, and $a_3 = 1,053\,\text{mm}^2$, after 16 iterations (see Fig. 17a). Figure 17b confirms that each group has at least one member with stress ratio equal to 1.0.

5.1.2 GSM solution

The initial domain extrusion assumes a flat configuration of the surface (i.e. $\bar{z} = 0$ everywhere), and is extruded to a height of 26 using 12 elements in thickness as shown in Fig. 18a. The structure is loaded by the self-weight of the panels, which is taken to be $q = 1\,\text{unit/m}^2$, and calculated based on the *current* surface configuration. After the optimal (pin-jointed) solution is found, a new surface is calculated (20) and the loads are updated. The domain is again extruded around the calculated surface, solved and updated a total of 6 times. With the exception of the very first domain, the surface is extruded equally in both directions. The extrusion thickness is continuously decreased throughout the iterations: the second domain is extruded to a total thickness of 13 and is shown in Fig. 18b; the sixth and final domain is extruded to a total thickness of 2.6 and can be seen in Fig. 18c. The interpolated surface obtained from the last iteration in the process is shown in Fig. 18d. The ground structure solution (Fig. 19a) provides information on the optimal load-path of the forces in the optimized grid-shell geometry, with the relative magnitude of these forces illustrated by the member thickness: the load-path hints at a mostly one-way structural system, with smaller members providing lateral support and resolving the perpendicular components. The resulting (interpolated) height shown in Fig. 19b does not depend on user-defined parameters, and it *closely* approximates the (tessellated) optimal shape.

5.1.3 FDM solution

The initial domain is discretized in the same manner as in the PEM solution (see Fig. 14). The force density is assigned as shown in Fig. 20, with $r_{unit} = 50$ kN/m.

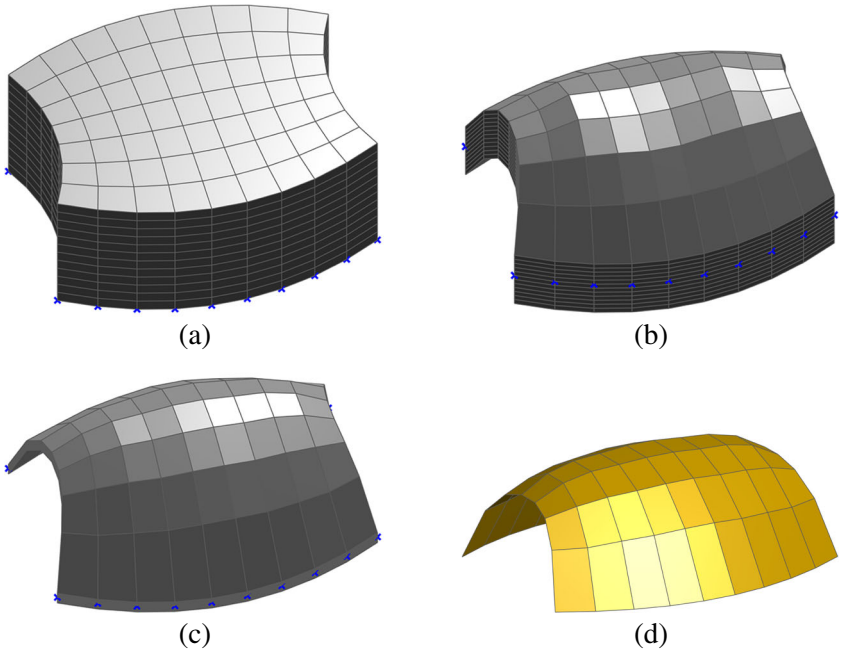

Fig. 18 Quadratic synclastic dome: domain discretizations used in the ground structure generation algorithm (GSM). **a** Initial discretization; **b** Domain discretization after the 1^{st} refinement; **c** Domain discretization after the 5^{th} refinement; **d** Final interpolated surface geometry

The form converges after 5 iterations, and the result is shown in Fig. 21. The geometric requirements are met with an apex height of 12.19 m and an opening height of 6.15 m. After this form-finding process, the members can be sized in the same manner as in the PEM method (if needed).

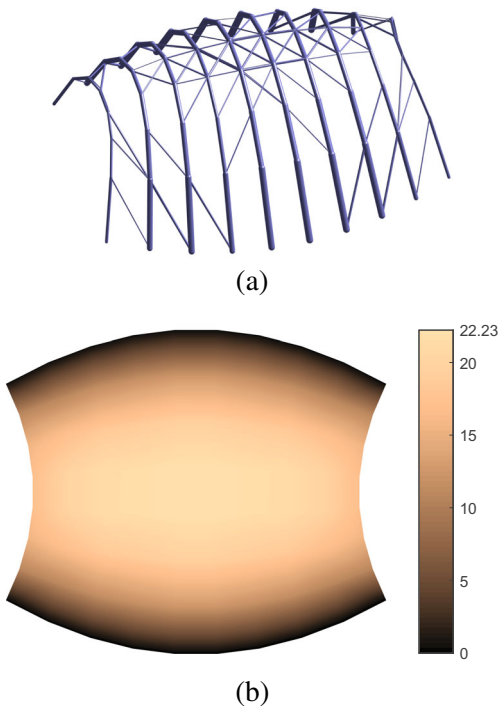

Fig. 19 Quadratic synclastic dome: optimized ground structure obtained after 5 domain refinements (6 analysis processes). **a** Member layout; **b** Optimized height

5.2 Polygonally tessellated pavilion

The second example is a polygonally tessellated pavilion with internal supports and multiple openings, which is illustrated by Figs. 22, 23, 24, 25, 26 and 27. The domain is discretized into polygonal panels in the XY plane using the educational software *PolyMesher* (Talischi et al. 2012). This example demonstrates that the proposed methods work with unstructured polygonal load panels, holes, and concavities.

5.2.1 PEM solution

Figure 22 shows the domain partition, consisting of 270 nodes, 138 load panels, and 369 bars (edges). The system is loaded by its panels, considering a self-weight load of

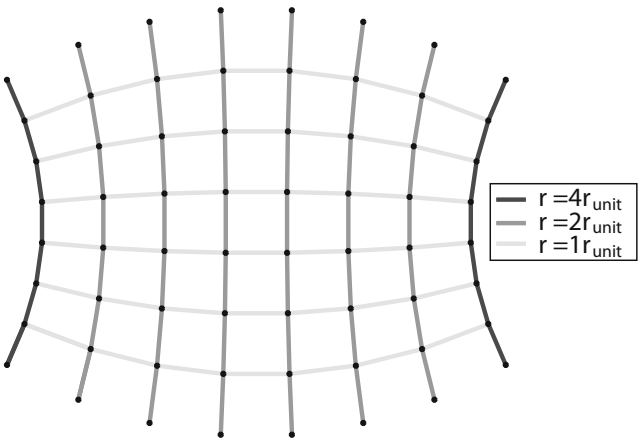

Fig. 20 Quadratic synclastic dome: user-defined force densities

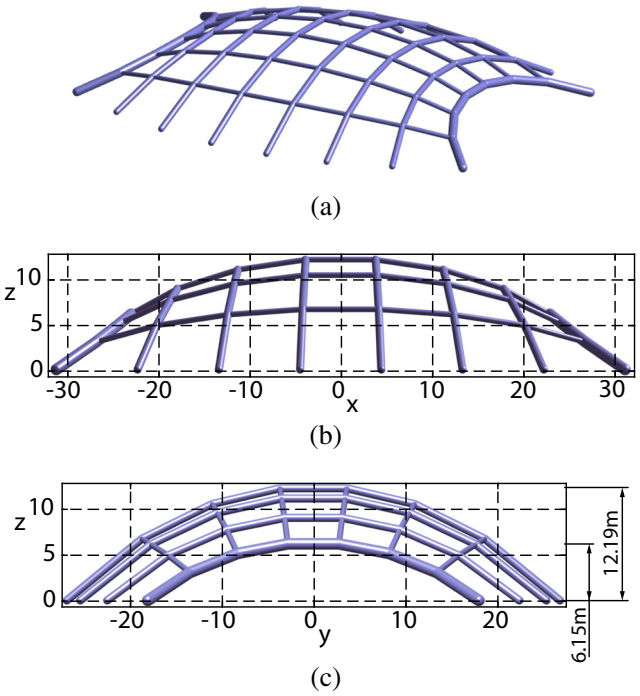

Fig. 21 Quadratic synclastic dome: form-finding result by FDM. **a** Isometric view; **b** Front view; **c** Side view

4.5 kN/m^2 and an upward wind suction load of 0.5 kN/m^2. The bars have an identical Young's modulus of 1 GPa and cross-sectional area of 120 mm^2. The isometric and front view of the resulting form after 5 iterations are shown in Fig. 23a and b, respectively. We observe that the apex occurs near the center of the domain with a height of 4.10 m.

Member sizing is done after the form-finding stage using the stress ratio method with a numerical damping of $\eta = 0.5$. The adopted material properties, admissible stress reduction and load combination are the same as used in Section 5.1.1. Starting with an initial guess of 5, 000 mm^2 for all cross-sections, the values converge to the

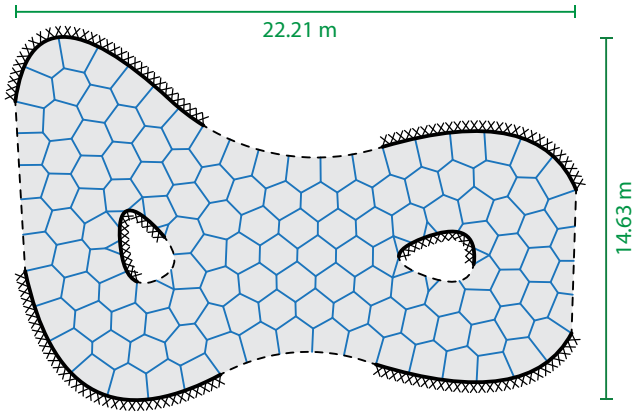

Fig. 22 Polygonally tessellated pavilion: footprint with load panel partition and support boundary conditions

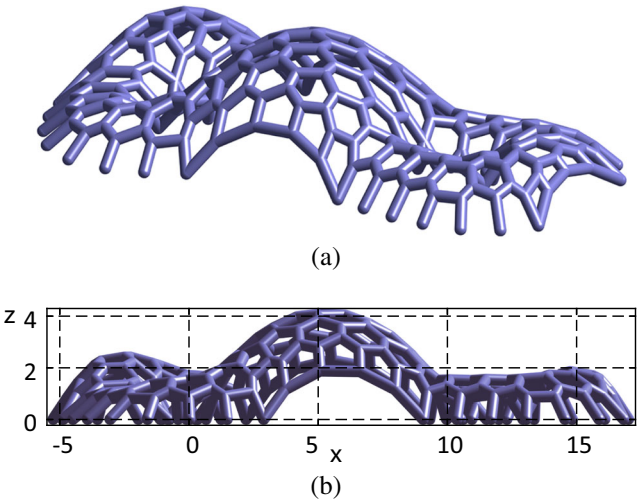

Fig. 23 Polygonally tessellated pavilion: form-finding result by the PEM. **a** Isometric view; **b** Front view

fully-stressed design shown in Fig. 24 after 115 iterations. The maximum cross-sectional area in the structure is 218 mm^2.

5.2.2 GSM solution

The initial domain extrusion assumes a flat configuration of the surface (i.e. $\bar{z} = 0$ everywhere), and is extruded to a height of 6 using 8 elements in thickness as shown in Fig. 25a. The structure is loaded by the self-weight of the panels, which is taken to be $q = 1$ unit/m^2, and calculated based on the *current* surface configuration. After the optimal (pin-jointed) solution is found, a new surface is calculated (20) and the loads are updated. The domain is again extruded around the calculated surface, solved and updated a total of 6 times. With the exception of the very first domain, the surface is extruded equally in both directions. The extrusion thickness is continuously decreased throughout the iterations: the second domain is extruded to

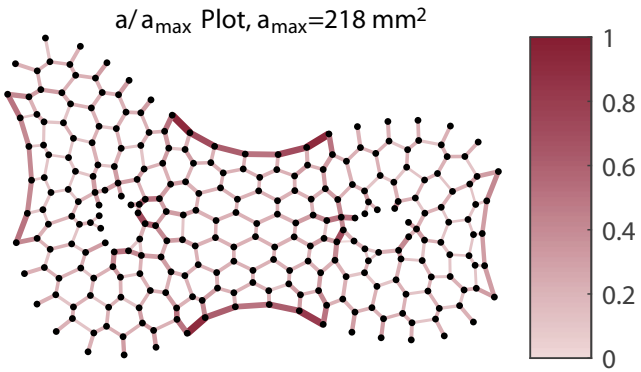

Fig. 24 Polygonally tessellated pavilion: area ratio plot based on the PEM solution

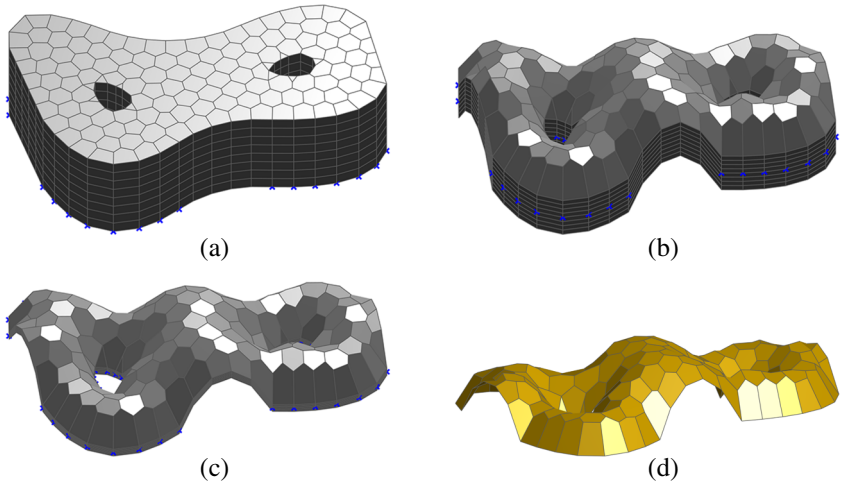

Fig. 25 Polygonally tessellated pavilion: domain discretizations used in the ground structure generation algorithm (GSM). **a** Initial discretization; **b** Domain discretization after the 1^{st} refinement; **c** Domain discretization after the 5^{th} refinement; **d** Final interpolated surface geometry.

a total thickness of 3 and is shown in Fig. 25b; the sixth and final domain is extruded to a total thickness of 0.6 and can be seen in Fig. 25c. The interpolated surface obtained from the last iteration in the process is shown in Fig. 25d. The ground structure solution (Fig. 26a) provides information on the optimal load-path of the forces in the optimized grid-shell geometry, with the relative magnitude of these forces illustrated by the member thickness. The resulting (interpolated) height shown in Fig. 26b does not depend on user-defined parameters, and it *closely* approximates the (tessellated) optimal shape.

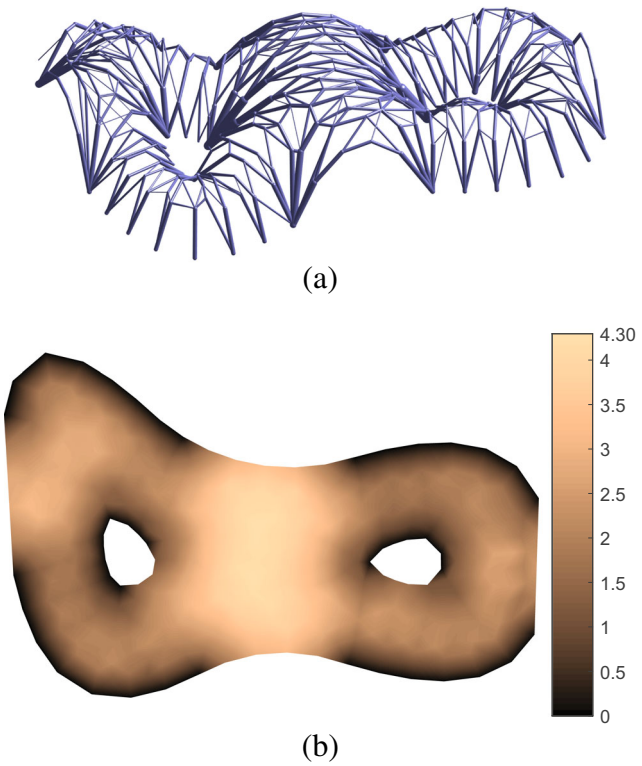

Fig. 26 Polygonally tessellated pavilion: optimized ground structure obtained after 5 domain refinements (6 analysis processes). **a** Member layout; **b** Optimized height

5.2.3 FDM solution

The FDM solution uses the same domain discretization as the PEM solution (see Fig. 22). A uniform force density of 15 kN/m is applied to all members. With this setup, the form converges after 6 iterations. Figure 27a and b show the isometric and front view of the resulting form, respectively. We observe that the apex occurs near the center of the domain and has a height of approximately 4.25 m.

5.3 Doubly-curved bowtie grid-shell

This example covers a doubly-curved bowtie-shaped *wavy* surface with a targeting apex height of 25 m approximately, which is illustrated by Figs. 28, 29, 30, 31, 32, 33, 34 and

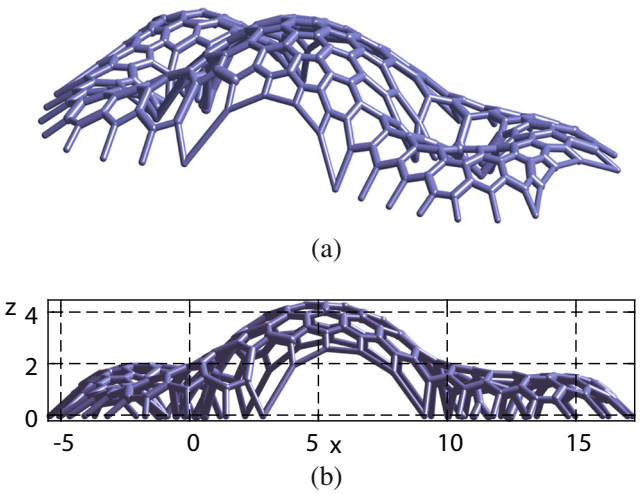

Fig. 27 Polygonally tessellated pavilion: form-finding result by the FDM. **a** Isometric view; **b** Front view

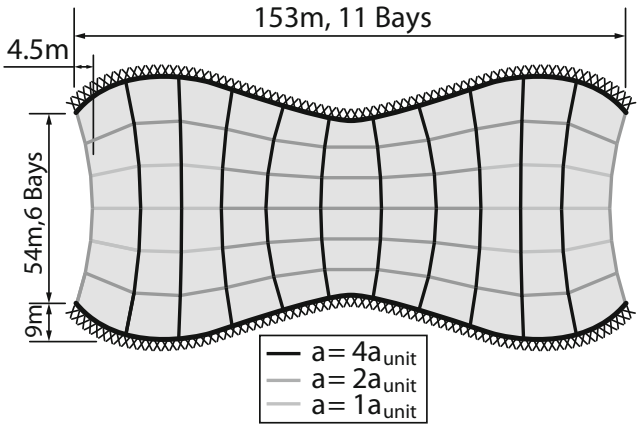

Fig. 28 Doubly-curved bowtie grid-shell: footprint, panel mesh, boundary conditions, and the prescribed cross-sectional areas used in the PEM. The prescribed cross-sectional areas used in the PEM adopt an a_{unit} value of 6, 000 mm^2

35. The grid-shell lies in a quasi-rectangular domain in the XY plane, with doubly curved longer edges and concave short edges. The edge geometry uses spline curves in its geometric definition and is shown to scale in Fig. 28.

5.3.1 PEM solution

The grid mesh is structured with 11 bays in the x-direction and 6 bays in the y-direction. The discretized domain shown in Fig. 28 is comprised of 84 nodes, 124 bars and 66 load panels. The constrained nodes are not flat on the ground (i.e. $z \neq 0$ m), but can be 9 m away from the ground level. The system is loaded by its panels, considering a self-weight load of 4.5 kN/m^2 and an upward wind suction load of 0.5 kN/m^2. The initial interior nodes' height (z direction) is interpolated from the exterior boundary in a smooth manner: a user-defined initial condition to achieve a desired form. The varying nodal elevations in the initial configuration cause the structure to have compressive local equilibrium conditions: i.e. the snap-through relaxation is necessary to achieve a tension-only form. Due to symmetry, the resulting form is expected to have a doubly-curved surface with two apexes aligned along the x axis. In addition to the domain specification, Fig. 28 also shows the cross-sectional areas of the members in the form-finding process, with $a_{unit} = 6,000\,\text{mm}^2$. All bars share the identical Young's modulus of 1 GPa.

The resulting form is obtained after 5 iterations, and is shown in Fig. 29. To better illustrate the variable height supports, the final configuration is shown with the columns that prop the grid-shell in said position. We observe that the form is indeed doubly-curved as desired, with a symmetric apex height of 24.99 m, and an opening height of 13.90 m, both measured from the zero level.

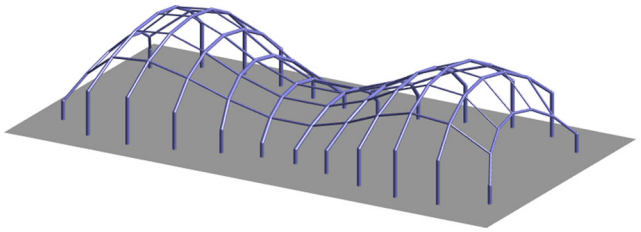

Fig. 29 Doubly-curved bowtie grid-shell: isometric view of the PEM form. Note that the grid-shell support columns are plotted only to show height fluctuation of boundary nodes, but they are not part of analysis nor optimization

The member sizing is done after the form-finding stage using the stress ratio method with a numerical damping of $\eta = 0.5$. The adopted material properties, admissible stress reduction and load combination are the same as used in Section 5.1.1. The member sizing results are plotted in Fig. 30, with a maximum cross-sectional area of 13, 515 mm^2.

5.3.2 GSM solution

The initial domain extrusion assumes a flat configuration of the surface (i.e. $\bar{z} = 0$ everywhere), and is extruded to a height of 24 using 10 elements in thickness as shown in Fig. 31a. The structure is loaded by the self-weight of the panels equal to 4.5 kN/m^2 and an upward wind suction of 0.5 kN/m^2, both calculated based on the *current* surface configuration.

After the optimal (pin-jointed) solution is found, a new surface is calculated (20) and the loads are updated. The domain is again extruded around the calculated surface, solved and updated a total of 6 times. With the exception of the very first domain, the surface is extruded equally in both directions. The extrusion thickness is continuously decreased throughout the iterations: the second domain is extruded to a total thickness of 12 and is shown in Fig. 31b; the sixth and final domain is extruded to total thickness of 2.4 and can be seen in Fig. 31c. The interpolated surface obtained from the last iteration in the process is shown

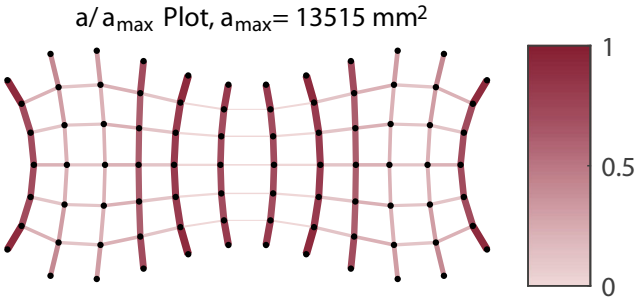

Fig. 30 Doubly-curved bowtie grid-shell: area ratios based on the PEM form

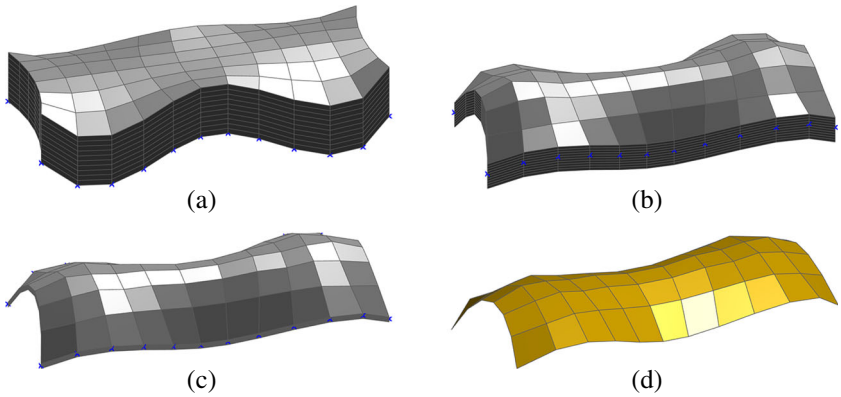

Fig. 31 Doubly-curved bowtie grid-shell: domain discretizations used in the ground structure generation algorithm (GSM). **a** Initial discretization; **b** Domain discretization after the 1^{st} refinement; **c** Domain discretization after the 5^{th} refinement; **d** Final interpolated surface geometry.

in Fig. 31d. The ground structure solution (Fig. 32a) provides information on the optimal load-path of the forces in the optimized grid-shell geometry, with the relative magnitude of these forces illustrated by the member thickness: the surface works as two independent synclastic domes interconnected by an anticlastic region in the middle; i.e. there is (relatively) no force exchange between the two synclastic regions. The resulting (interpolated) height shown in Fig. 32b does not depend on user-defined parameters, and it *closely* approximates the (tessellated) optimal shape.

Symmetry of the interpolated surface is enforced in this problem. The numerical nature of the interior-point method solver, which stops (within some tolerance) before reaching an absolute vertex of the feasible domain, together with the relative *flatness* of the objective near the optimum, cause the symmetry of this problem to be lost. This loss of symmetry is unnoticeable after a single step. However, after the series of 6 domain refinements, load updates, optimization and interpolation steps, this asymmetry is accentuated (note the minor differences in Fig. 32a). Thus, for a symmetric problem (like the one addressed here), it is recommended to enforce symmetry of the interpolated surface.

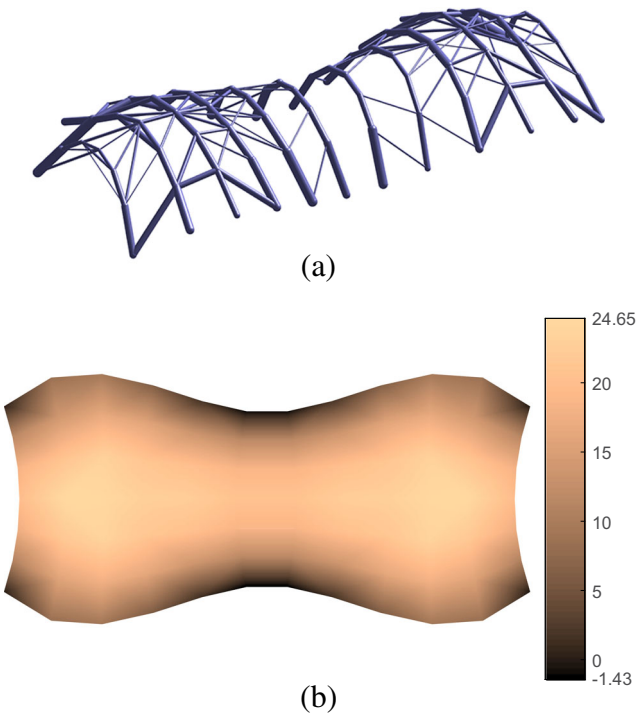

Fig. 32 Doubly-curved bowtie grid-shell: optimized ground structure obtained after 5 domain refinements (6 analysis processes). **a** Member layout; **b** Optimized height

5.3.3 FDM solution

The FDM process uses the same domain discretization as in the PEM section (see Fig. 28). The force density of all bars is defined as 106 kN/m. The resulting form converges after 7 iterations and is shown in Fig. 33. As done for the PEM form, the final configuration is shown with the columns that prop the grid-shell in said position to better illustrate the variable height supports. We observe that the form is indeed doubly-curved as desired, with an symmetric apex height of 24.98 m, and an opening height of 19.60 m, both measured from the zero level.

5.3.4 Convergence history

In the form-finding process, the nodal loads are design-dependent. Thus, iterations are needed to obtain a converged form. The convergence history for the bowtie example is shown in Fig. 34. For the PEM and FDM, the result

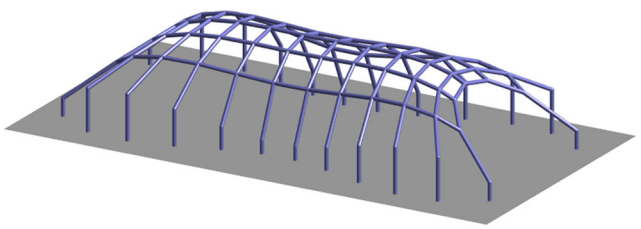

Fig. 33 Doubly-curved bowtie grid-shell: isometric view of FDM form. Note that the grid-shell support columns are plotted only to show height fluctuation of boundary nodes, but they are not part of analysis nor optimization

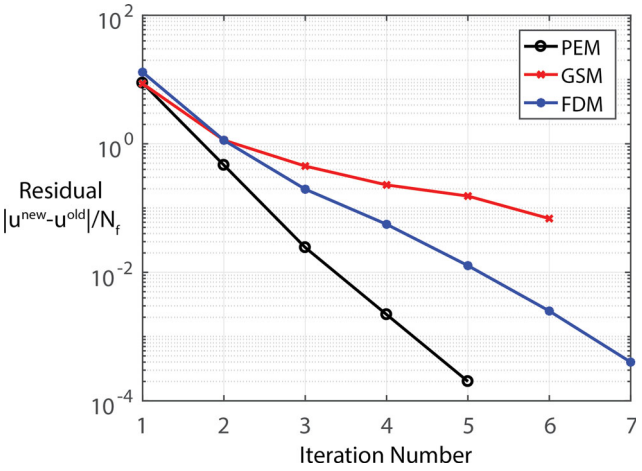

Fig. 34 Doubly-curved bowtie grid-shell: convergence history for the form-finding methods (PEM, GSM, and FDM)

converges after 5 and 7 iterations, respectively. Convergence is achieved once the residual (2) is less than a specified tolerance. For the bowtie example, $N_f = 180$ and $\epsilon = 10^{-3}$. For the GSM, a specific number of iterations (6) is specified, and the residual is evaluated.

5.3.5 Layout investigation

Figure 35 shows the PEM, GSM and FDM form of the doubly-curved bowtie grid-shell considering XY (plane view) and XZ (front view) projections. Note that the GSM form is obtained using the interpolated surface with a structured mesh similar to the PEM and FDM form. In the left column of Fig. 35, the red dashed line denotes the horizontal location (along Y dirction) of the top of the left edge arch in the FDM form diagram. We observe that the FDM form diagram has a smaller footprint as the edge arch curves significantly towards the center. In the right column of Fig. 35, the dark dashed lines denote the apex heights. We observe that the PEM form diagram is the least vaulted in the sense that in the front view, most of the top boundary is lower than the apex height. On the other hand, the FDM form diagram is the most vaulted, and the GSM form diagram is in between the other two diagrams.

5.3.6 Tonnage evaluation and comparison among the methods

From a design point of view, the effectiveness of a layout can be evaluated by the material tonnage. The closer to the optimal layout the design is, the lower the tonnage. Here we use preliminary member sizing results to estimate (a lower bound of) the material tonnage. Table 2 shows the estimated tonnages and the vertical load sums for the three forms obtained by PEM, GSM and FDM for the doubly-curved bowtie grid-shell.

From Table 2, we observe that the GSM form requires the least material tonnage among the three forms. In addition, the load sums are different as load forces are dependent on the geometry. The load sums of the PEM form and the GSM

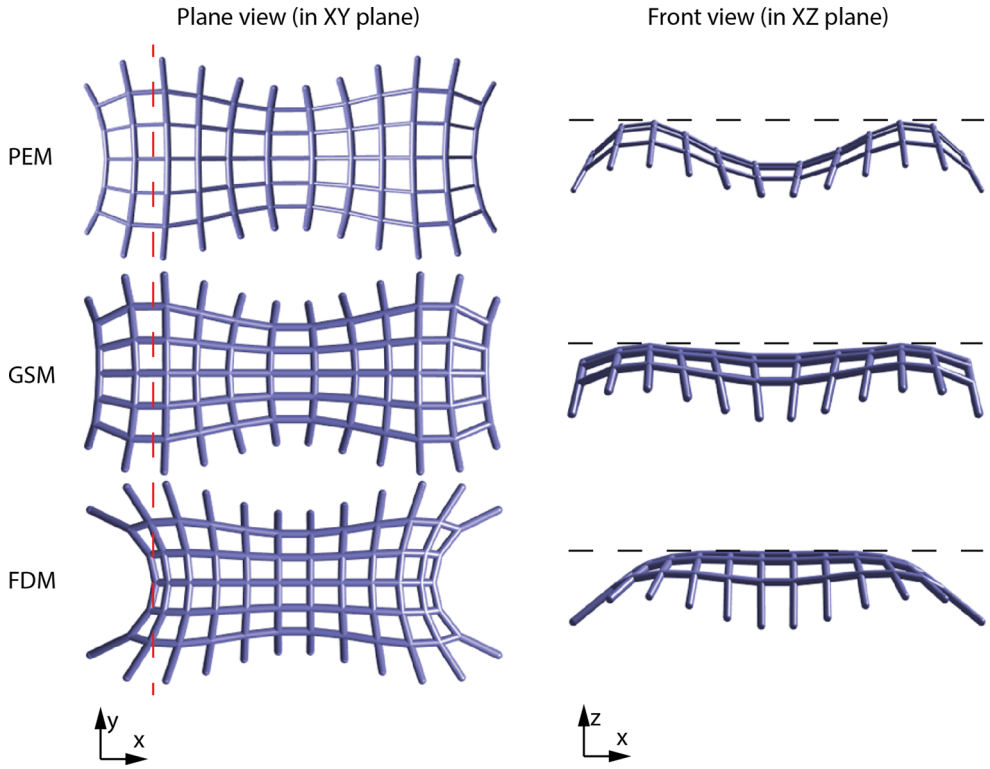

Fig. 35 Doubly-curved bowtie grid-shell: comparison of the PEM, GSM and FDM form considering XY (plane view) and XZ (front view) projections

Table 2 Doubly-curved bowtie grid-shell: tonnage and load sum comparison of the designs obtained by the three form-finding methods

Method	PEM	GSM	FDM
Tonnage [ton]	71.1	63.2	71.9
Normalized Tonnage	1.12	1.00	1.14
Load sum [kN]	44629	45287	36515

The tonnage is calculated by multiplying the total material volume by the material density. Assume that the construction material is A500 Gr. B carbon steel with a density of 7.85 ton/m^3. The normalized tonnage is calculated by dividing the tonnage by the GSM tonnage

form are comparable. The vertical load summation of the FDM form is lower than the other two, because the FDM form has a smaller footprint. As a result, the total tributary area for load calculation is smaller. Comparing both the tonnage and the vertical load sum, we observe that the GSM form supports the largest vertical load with the least amount of material.

To understand why the GSM design is more efficient, we investigate several parameters related with the load path. One parameter of interest is the Michell number (Michell 1904), which is defined as $\sum |P| L$, where P is the member force (positive for tension)and L is the member length. Another important quantity, Maxwell number (Maxwell 1890), is defined as $\sum P \cdot L$. In our cases, the grid-shell is or is close to compression-only and thus the Michell number and the Maxwell number are of similar magnitudes. According to Maxwell's theorem (Maxwell 1890), the Maxwell number equals the sum of the force-distance product from all forces. Thus

$$\sum P \cdot L = \sum \mathbf{F}^T \mathbf{D} \tag{21}$$

where $\mathbf{F}$ is the external force vector and $\mathbf{D}$ is the distance vector pointing from an arbitrary origin to the point where the force $\mathbf{F}$ is applied. With the above definition, the concerned parameters are calculated and tabulated in Table 3. Specifically, we calculate the total force-distance product together with the components from the load forces and reaction forces, respectively.

First of all, we verify that the calculation is correct by noticing that the normalized tonnages are equal to the normalized Michell numbers. For fully-stressed truss structures, the Michell number is linearly correlated with the material volume (Baker et al. 2013), as

$$\sum |P| L = \sum \sigma_{adm} A L = \sigma_{adm} \sum AL = \sigma_{adm} V \tag{22}$$

where A denotes the member cross sectional area and V is the total material volume. Similarly, the tonnage is also linearly correlated with V, as

$$\text{Tonnage} = \rho V \tag{23}$$

Table 3 Doubly-curved bowtie grid-shell: Michell number, Normalized Michell number, Maxwell number and force-distance product of the designs obtained by the three form-finding methods

Method	PEM	GSM	FDM
Michell Number [kN · m]	2.57×10^6	2.29×10^6	2.60×10^6
Normalized Michell number	1.12	1.00	1.14
Maxwell number [kN · m]	-2.57×10^6	-2.28×10^6	-2.60×10^6
Force-distance product [kN · m]	-2.57×10^6	-2.28×10^6	-2.60×10^6
Force-distance product from load forces [kN · m]	-6.83×10^5	-8.32×10^5	-7.11×10^5
Force-distance product from reaction forces [kN · m]	-1.89×10^6	-1.44×10^6	-1.89×10^6

The normalized Michell number is calculated by dividing the Michell number by the GSM Michell number

where ρ is the material density. Thus the normalized tonnage should be equal to the normalized Michell number if the calculation is correct.

From Table 3, we observe that the GSM form provides the least magnitude of the force-distance product (equivalently, the Michell number or the magnitude of the Maxwell number) among the three forms. Due to the large load sum and relatively vaulted form, the GSM form has the largest magnitude of the force-distance product from load forces. However, the GSM form results in smaller reaction forces in the XY plane than the other two forms, and its force-distance product from reaction forces is also smaller. Overall, the total force-distance product of the GSM form is still smaller than that of the other forms. Thus, we conclude that the structural efficiency of the GSM form comes from the more benign horizontal reaction forces.

6 Discussion

Several aspects can influence the choice of the form-finding method. One aspect of concern is the computational

Table 4 Computational cost of the form-finding methods used in the numerical examples section. The computational costs are measured in real time in seconds [a]

Method	PEM	GSM	FDM
Dome	2	1168	0.1
Pavilion	17	19635	0.3
Bowtie	4	773	0.2

[a]The computations were conducted using MATLAB R2015b on a desktop computer with an Intel® Xeon® CPU E5-1660 v3 @ 3.00GHz processor and an installed memory (RAM) of 64 GB

Table 5 Qualitative comparison of the form-finding methods presented

Method	PEM	GSM	FDM
Computational complexity	moderate	heavy	mild
Physics	equilibrium, mechanics, and compatibility	equilibrium	equilibrium
Initial configuration dependency	yes	no	no
Pre-defined connectivity	yes	no	yes

complexity, which can be preliminarily evaluated by means of the computational runtime as shown in Table 4. This aspect, as well as other metrics of interest are qualitatively compared in Table 5.

In summary, the PEM yields solutions with full physical consideration of the standard constitutive relationships. Thus, all the parameters required have direct physical meanings, and the method can be easily understood from an intuitive point of view. A key drawback of the method is the dependence of the resulting form on the initial configuration. However, it may also be argued that this dependence can be exploited to drive the solution towards some desirable form.

The GSM with transmissible loads requires no a priori assumption on the geometry nor the member connectivity, thus making it the most agnostic of the three methods. However, it ranks high in computational complexity and requires interpretation (or rationalization) of the results. The resulting configuration does not depend on additional parameters such as member stiffness or force density; it only requires the footprint geometry. In other words, for a given problem, the method converges to a unique grid-shell configuration.

The FDM is the most computationally inexpensive of the three form-finding methods. A major drawback of FDM is that the *force density*, a parameter that the method heavily relies on, may not have a clear physical interpretation. Therefore, the outcome from the FDM is relatively hard to predict and control, relying on the user's experience or some degree of *trial-and-error*. While the FDM does not depend on the initial configuration, connectivity information is still required (see Appendix A for further information).

7 Concluding remarks

In this paper, two form-finding methods for grid-shell designs are proposed: a method based on *minimum potential energy*, and a method based on an augmented form of the *ground structure method*, including domain refinement. The load derivation scheme used in the present work allows for various types of static loads, which can be applied to load panels, bar members, and/or directly at the nodes. These loads can be design-dependent, and thus the form-finding process is iterative. The results from the two proposed form-finding methods, together with the widely-known *force density method*, were compared with three design examples. These examples demonstrate the capability of the form-finding methods to handle various load types, unstructured domains, and polygonal discretizations. In particular, we investigate the layout and tonnage for the doubly-curved bowtie grid-shell to compare the structural efficiency of the forms obtained with different methods.

Last but not least, we note that the three form-finding methods (two proposed and one reviewed) do not consider buckling in their form-finding nor sizing stages. Consideration for elastic buckling can be integrated into the proposed methods provided that a section family is defined (refer to Section 3.4). However, the results should be considered as an *initial approach* towards a complete design, which complies with local building codes (e.g. International Code Council 2015; ACI Committee 318, American Concrete Institute 2014; American Institute of Steel Construction 2011).

Acknowledgments The authors acknowledge the financial support from the US National Science Foundation (NSF) under projects #1559594 (formerly #1335160), which is a GOALI (Grant Opportunities for Academic Liaison with Industry) project with SOM (Skidmore, Owings & Merrill LLP), and project #1321661. Ms Haley Simms provided valuable comments that contributed to improve the manuscript. We are also grateful for the endowment provided by the Raymond Allen Jones Chair at the Georgia Institute of Technology. The information provided in this paper is the sole opinion of the authors and does not necessarily reflect the views of the sponsoring agencies.

Appendix A: Force density method formulation

The formulation of the force density method presented here follows the procedure in Schek (1974), and is presented here for the sake of completeness.

The nodes are numbered from 1 to N_n and bar members (or branches) from 1 to N_b. For any bar member j, there are 2 corresponding nodes with number c_j and d_j. The $N_b \times N_n$ branch-node matrix $\mathbf{C}_s$ is constructed as follows:

$$\mathbf{C}_s(j,i) = \begin{cases} +1 & \text{for } c_j = i \\ -1 & \text{for } d_j = i \\ 0 & \text{otherwise} \end{cases} \tag{24}$$

The branch-node matrix $\mathbf{C}_s$ can be subdivided into $\mathbf{C}$ and $\mathbf{C}_f$, which corresponds to the columns associated with free

and fixed nodes, respectively. The unknown nodal coordinates are defined as $\mathbf{x}$, $\mathbf{y}$, and $\mathbf{z}$; and the coordinates of the fixed nodes as $\mathbf{x}_f$, $\mathbf{y}_f$ and $\mathbf{z}_f$. The vectors denoting the coordinate difference between 2 connected nodes are $\mathbf{u}$, $\mathbf{v}$, and $\mathbf{w}$ (in the x, y and z coordinates respectively). Thus, the relations between the nodal coordinates and the coordinate differences are:

$$\begin{aligned}\mathbf{u} &= \mathbf{C}\mathbf{x} + \mathbf{C}_f\mathbf{x}_f \\ \mathbf{v} &= \mathbf{C}\mathbf{y} + \mathbf{C}_f\mathbf{y}_f \\ \mathbf{w} &= \mathbf{C}\mathbf{z} + \mathbf{C}_f\mathbf{z}_f\end{aligned} \tag{25}$$

For each element j in the network its length is calculated as $\ell_j = \sqrt{u_j^2 + v_j^2 + w_j^2}$, and its force density is defined as $q_j = n_j/\ell_j$, where n_i is the member internal force. The member lengths are grouped in a vector $\boldsymbol{\ell}$, the member forces in $\mathbf{n}$, and the user-defined force densities for all members in the network in $\mathbf{q}$.

We denote the diagonal matrices of vectors $\mathbf{u}$, $\mathbf{v}$, $\mathbf{w}$, $\boldsymbol{\ell}$ and $\mathbf{q}$ as $\mathbf{U}$, $\mathbf{V}$, $\mathbf{W}$, $\mathbf{L}$ and $\mathbf{Q}$. The nodal force equilibrium can then be expressed as:

$$\begin{aligned}\mathbf{C}^T\mathbf{U}\mathbf{L}^{-1}\mathbf{n} &= \mathbf{f}_x \\ \mathbf{C}^T\mathbf{V}\mathbf{L}^{-1}\mathbf{n} &= \mathbf{f}_y \\ \mathbf{C}^T\mathbf{W}\mathbf{L}^{-1}\mathbf{n} &= \mathbf{f}_z\end{aligned} \tag{26}$$

where $\mathbf{f}_x$, $\mathbf{f}_y$, and $\mathbf{f}_z$, are the nodal force vectors in the x, y and z coordinates, respectively. Using the definition of force density in (26) we obtain:

$$\begin{aligned}\mathbf{C}^T\mathbf{U}\mathbf{q} &= \mathbf{f}_x \\ \mathbf{C}^T\mathbf{V}\mathbf{q} &= \mathbf{f}_y \\ \mathbf{C}^T\mathbf{W}\mathbf{q} &= \mathbf{f}_z\end{aligned} \tag{27}$$

where a simple transformation gives:

$$\begin{aligned}\mathbf{U}\mathbf{q} &= \mathbf{Q}\mathbf{u} \\ \mathbf{V}\mathbf{q} &= \mathbf{Q}\mathbf{v} \\ \mathbf{W}\mathbf{q} &= \mathbf{Q}\mathbf{w}\end{aligned} \tag{28}$$

Using the definition of coordinate difference (25) and the definitions in (27) and (28), we obtain:

$$\begin{aligned}\mathbf{C}^T\mathbf{Q}\mathbf{C}\mathbf{x} + \mathbf{C}^T\mathbf{Q}\mathbf{C}_f\mathbf{x}_f &= \mathbf{f}_x \\ \mathbf{C}^T\mathbf{Q}\mathbf{C}\mathbf{y} + \mathbf{C}^T\mathbf{Q}\mathbf{C}_f\mathbf{y}_f &= \mathbf{f}_y \\ \mathbf{C}^T\mathbf{Q}\mathbf{C}\mathbf{z} + \mathbf{C}^T\mathbf{Q}\mathbf{C}_f\mathbf{z}_f &= \mathbf{f}_z\end{aligned} \tag{29}$$

Finally, defining the matrix $\mathbf{D}$ as $\mathbf{D} = \mathbf{C}^T\mathbf{Q}\mathbf{C}$, and $\mathbf{D}_f$ as $\mathbf{D}_f = \mathbf{C}^T\mathbf{Q}\mathbf{C}_f$, a linear system for the free (unknown) nodal coordinates that ensures force equilibrium at every node is obtained:

$$\begin{aligned}\mathbf{D}\mathbf{x} &= \mathbf{f}_x - \mathbf{D}_f\mathbf{x}_f \\ \mathbf{D}\mathbf{y} &= \mathbf{f}_y - \mathbf{D}_f\mathbf{y}_f \\ \mathbf{D}\mathbf{z} &= \mathbf{f}_z - \mathbf{D}_f\mathbf{z}_f\end{aligned} \tag{30}$$

Appendix B: Nomenclature

$\mathbf{A}$	Correspondence matrix of nodes belonging to a transfer group
$\mathbf{a}$	Vector of member cross-sectional areas
$a_{ij}^{\triangle}$	Area of one single triangle associated with the edge nodes i and j
a_i^k	Cross-sectional area of the i-th bar in the k-th iteration
a_g^k	Cross-sectional area of bars in the g-th group in the k-th iteration
$\mathbf{B}^T$	Nodal equilibrium matrix
$\mathbf{D}$	Distance vector
$\mathbf{F}$	External force vector
$\mathbf{f}$	Nodal load vector
$\mathbf{f}_{xy}$	Nodal loads associated with the x and y coordinates
$\mathbf{f}_z$	Nodal loads associated with the z coordinate
$\mathbf{f}_v$	Vector of loads associated with each transfer group
$\mathbf{f}_i^{\bullet}$	Load vector applied directly at the i-th node
$\mathbf{f}_i^{\diagup}$	Line loads associated with the edges
$\mathbf{f}_i^{\square}$	Area loads associated with the load panels
$\tilde{k}_i$	Reduced bar stiffness for the i-th member used in the PEM form-finding process
k_i	Real bar stiffness for the i-th member
L	Member length
$\boldsymbol{\ell}$	Vector of member lengths
$\Delta\ell_i$	Length change for the i-th member
N_f	Number of degrees of freedom
$\mathbf{n}$	Vector of member forces
$\mathbf{n}_{ij}^{\triangle}$	Unit normal vector of the triangle associated with the edge nodes i and j
P	Member force
PE	Potential Energy
$\mathbf{q}$	Self weight by unit area
$\mathbf{s}^+$	Slack variables associated with tension
$\mathbf{s}^-$	Slack variables associated with compression
$\mathbf{u}$	Displacement vector
$\mathbf{u}^{\text{new}}$	Displacement vector in the current iteration
$\mathbf{u}^{\text{old}}$	Displacement vector in the previous iteration
$\mathbf{v}_i$	Vector from a polygon's center of mass to the i-th node
V	Material volume of the resulting structure
$\mathbf{w}$	Projected area load acting on the load panels
β	Transfer group's load direction vector
γ	Material specific weight of the bar members
η	Numerical damping for the stress-ratio method
κ	Ratio of tension to compression stress limit, i.e. σ_T/σ_C
ρ	Material density of the bar members
$\sigma_{adm,i}$	Admissible stress associated with the i-th bar
σ_i	Stress in the i-th bar
σ_C	Compression stress limit
σ_T	Tension stress limit

References

ACI Committee 318, American Concrete Institute (2014) Building Code Requirements for Structural Concrete (ACI 318-14) and Commentary (ACI 318R-14)

Addis B (2007) Building: 3000 years of design, engineering and construction. Phaidon Press, London

Akbarzadeh M, Van Mele T, Block P (2015) Spatial compression-only form finding through subdivision of external force polyhedron. In: Proceedings of the international association for shell and spatial structures (IASS). Symposium, Amsterdam

American Institute of Steel Construction (2011) Steel Construction Manual. 14th Edn

Argyris JH, Angelopoulos T, Bichat B (1974) A general method for the shape finding of lightweight tension structures. Comput Methods Appl Mech Eng 3:135–149

Baker WF (1992) Energy-based design of lateral systems. Struct Eng Int 2(2):99–102

Baker WF, Beghini LL, Mazurek A, Carrion J, Beghini A (2013) Maxwell's reciprocal diagrams and discrete Michell frames. Struct Multidiscip Optim 48:267–277

Barnes MR (1977) Form-finding and analysis of tension space structures by dynamic relaxation. PhD Thesis, City University London

Barnes MR (1988) Form-finding and analysis of prestressed nets and membranes. Comput Struct 30(3):685–695

Barnes MR, Topping BHV, Wakefield DS (1977) Aspects of form-finding by dynamic relaxation. In: International conference on the behaviour of slender structures

Bendsøe MP, Ben-Tal A, Zowe J (1994) Optimization methods for truss geometry and topology design. Struct Multidiscip Optim 7(3):141–159

Bendsøe MP, Sigmund O (2003) Topology optimization: theory, methods, and applications. Springer, Berlin

Bergós J, Llimargas M (1999) Gaudí: The Man and His Work. Taschen, Köln

Bletzinger K-U, Ramm E (1993) Form finding of shells by structural optimization. Eng Comput 9(1):27–35

Bletzinger K-U, Ramm E (1999) A general finite element approach to the form finding of tensile structures by the upyeard reference strategy. Int J Space Struct 14(2):131–145

Bletzinger K-U, Ramm E (2001) Structural optimization and form finding of light weight structures. Comput Struct 79(22):2053–2062

Bletzinger K-U, Wüchner R, Daoud F, Camprubí N (2005) Computational methods for form finding and optimization of shells and membranes. Comput Methods Appl Mech Eng 194(30):3438–3452

Block P (2009) Thrust network analysis: exploring three-dimensional equilibrium. PhD thesis, Massachusetts Institute of Technology, USA

Block P, Ochsendorf J (2007) Thrust network analysis: a new methodology for three-dimensional equilibrium. J Intern Assoc Shell Spatial Struct 48(3):167–173

Chiandussi G, Codegone M, Ferrero S (2009) Topology optimization with optimality criteria and transmissible loads. Comput Math Appl 57(5):772–788

Chilton J (2010) Heinz Isler's infinite spectrum form-finding in design. Archit Des 80(4):64–71

Christensen PW, Klarbring A (2009) An introduction to structural optimization, vol 153 of solid mechanics and its applications. Springer Netherlands, Dordrecht

Coelho RF, Tysmans T, Verwimp E (2014) Form finding & structural optimization. Struct Multidiscip Optim 49(6):1037–1046

Collins GR (1977) The Drawings of Antonio gaudí. The drawing center, New York

Darwich W, Gilbert M, Tyas A (2010) Optimum structure to carry a uniform load between pinned supports. Struct Multidiscip Optim 42(1):33–42

Dorn W, Gomory R, Greenberg H (1964) Automatic design of optimal structures. J de mécanique 3(1):25–52

Fuchs MB, Moses E (2000) Optimal structural topologies with transmissible loads. Struct Multidiscip Optim 19(4):263–273

Gallagher RH, Zienkiewicz OC (1973) Optimum structural design: theory and applications. Wiley, London

Gilbert M, Darwich W, Tyas A, Shepherd P (2005) Application of large-scale layout optimization techniques in structural engineering practice. In: 6th world congress of structural and multidisciplinary optimization, June 1–10

Haber R, Abel J (1982) Initial equilibrium solution methods for cable reinforced membranes part I-formulations. Comput Methods Appl Mech Eng 30(3):263–284

Hemp W (1973) Optimum structures, 1st edn. Oxford University Press, Oxford

International Code Council (2015) 2015 International Building Code

Jiang Y (2015) Free form finding of grid shell structures. Master's thesis, University of Illinois at Urbana-Champaign, USA

Karmarkar N (1984) A new polynomial-time algorithm for linear programming. Combinatorica 4(4):373–395

Kilian A, Ochsendorf J (2006) Particle spring systems for structural form finding. J Intern Assoc Shell Spatial Struct 46(2):77–84

Leon SE, Paulino GH, Pereira A, Menezes IFM, Lages EN (2011) A unified library of nonlinear solution schemes. Appl Mech Rev 64(4):040803

Lewiński T, Rozvany GIN, Sokół T, Bołbotowski K (2013) Exact analytical solutions for some popular benchmark problems in topology optimization III: L-shaped domains revisited. Struct Multidiscip Optim 47(6):937–942

Lewiński T, Zhou M, Rozvany GIN (1994) Extended exact solutions for least-weight truss layouts—Part I: cantilever with a horizontal axis of symmetry. Int J Mech Sci 36(5):375–398

Lewis WJ (2003) Tension structures: form and behaviour. Thomas Telford Publishing, London

Linkwitz K, Schek H (1971) Einige Bemerkungen zur Berechnung von vorgespannten Seilnetzkonstruktionen. Ingenieur-Archiv 40(3):145–158

Martinell C, Collins GR, Rohrer J (1975) Gaudí: his life, his theories, his work. MIT Press, Cambridge

Maxwell JC (1890) In: Niven WD (ed) The scientific papers of James Clerk Maxwell. Library Collection, Cambridge

Michell A (1904) The limits of economy of material in frame structures. Phil Mag 8(47):589–597

Miki M, Adriaenssens S, Igarashi T, Kawaguchi K (2014) The geodesic dynamic relaxation method for problems of equilibrium with equality constraint conditions. Int J Numer Methods Eng 99:682–710

Mitchell T (2013) A limit of eonomy of material in shell structures. PhD thesis, University of California Berkeley, USA

Nouri-Baranger T (2004) Computational methods for tension-loaded structures. Arch Comput Meth Eng 11(2003):143–186

Pauletti RMO, Pimenta PM (2008) The natural force density method for the shape finding of taut structures. Comput Methods Appl Mech Eng 197(49):4419–4428

Pichugin A, Tyas A, Gilbert M (2012) On the optimality of Hemp's arch with vertical hangers. Struct Multidiscip Optim 46(1):17–25

Ramos AS, Paulino GH (2015) Convex topology optimization for hyperelastic trusses based on the ground-structure approach. Struct Multidiscip Optim 51(2):287–304

Richardson JN, Adriaenssens S, Coelho RF, Bouillard P (2013) Coupled form-finding and grid optimization approach for single layer grid shells. Eng Struct 52:230–239

Rozvany GIN (2001) On design-dependent constraints and singular topologies. Struct Multidiscip Optim 21(2):164–172

Rozvany GIN, Gollub W, Zhou M (1997) Exact Michell layouts for various combinations of line supports-Part II. Struct Optim 14(2-3):138–149

Rozvany GIN, Prager W (1979) A new class of structural optimization problems: optimal archgrids. Comput Methods Appl Mech Eng 19(1):127–150

Rozvany GIN, Sokół T (2013) Validation of numerical methods by analytical benchmarks, and verification of exact solutions by numerical methods. Topology Optimization in Structural and Continuum Mechanics

Rozvany GIN, Wang CM (1983) On plane Prager-structures—I. Int J Mech Sci 25(7):519–527

Rozvany GIN, Wang CM, Dow M (1982) Prager-structures: Archgrids and cable networks of optimal layout. Comput Methods Appl Mech Eng 31(1):91–113

Sánchez J, Serna MÁ, Morer P (2007) A multi-step force–density method and surface-fitting approach for the preliminary shape design of tensile structures. Eng Struct 29(8):1966–1976

Schek HJ (1974) The force density method for form finding and computation of general networks. Comput Methods Appl Mech Eng 3(1):115–134

Siev A, Eidelman J (1964) Stress analysis of prestressed suspended roofs. J Struct Div 90(4):103–122

Sokół T (2011) A 99 line code for discretized Michell truss optimization written in Mathematica. Struct Multidiscip Optim 43(2):181–190

Sokół T (2014) Multi-load truss topology optimization using the adaptive ground structure approach. In: Łodygowski T, Rakowski J, Litewka P (eds) Recent advances in computational mechanics. CRC Press, Boca Raton, pp 9–16

Sokół T, Rozvany GIN (2013) On the adaptive ground structure approach for the multi-load truss topology optimization. In: 10th world congress on structural and multidisciplinary optimization, pp 1–10

Tabarrok B, Qin Z (1992) Nonlinear analysis of tension structures. Comput Struct 45(5):973–984

Talischi C, Paulino GH, Pereira A, Menezes IFM (2012) Polymesher: a general-purpose mesh generator for polygonal elements written in Matlab. Struct Multidiscip Optim 45:309–328

Thrall AP, Billington DP, Bréa KL (2012) The Maria Pia Bridge: A major work of structural art. Eng Struct 40:479–486

Tyas A, Pichugin AV, Gilbert M (2010) Optimum structure to carry a uniform load between pinned supports: exact analytical solution. Proc R Soc A Math Phys Eng sciences 467(2128):1101–1120

Veenendaal D, Block P (2012) An overview and comparison of structural form finding methods for general networks. Int J Solids Struct 49(26):3741–3753

Wang CM, Rozvany GIN (1983) On plane prager-structures—II: non-parallel external loads and allowances for selfweight. Int J Mech Sci 25(7):529–541

Wright M (2004) The interior-point revolution in optimization: history, recent developments, and lasting consequences. Bull Am Math Soc 42(01):39–56

Yang XY, Xie YM, Steven GP (2005) Evolutionary methods for topology optimisation of continuous structures with design dependent loads. Comput Struct 83(12-13):956–963

Zalewski W, Allen E (1997) Shaping structures: statics. Wiley, New York

Zegard T (2014) Structural optimization: from continuum and ground structures to additive manufacturing. PhD thesis, University of Illinois at Urbana-Champaign, USA

Zegard T, Paulino GH (2014) GRAND — Ground Structure based topology optimization for arbitrary 2D domains using MATLAB. Struct Multidiscip Optim 50(5):861–882

Zegard T, Paulino GH (2015) GRAND3 — Ground Structure based topology optimization for arbitrary 3D domains using MATLAB. Struct Multidiscip Optim 52(6):1161–1184

Zhang Y (1996a) Solving large-scale linear programs by interior-point methods under the MATLAB Environment. Technical report, Department of Mathematics and Statistics University of Maryland, Baltimore, USA

Zhang Y (1996b) Solving large-scale linear programs by interior-point methods under the Matlab Environment. Optim Methods Softw 10(1):1–31